Sensitivity of CCN spectra on chemical and physical properties of aerosol: A case study from the Amazon Basin

Gregory C. Roberts,[1,2] Paulo Artaxo,[3] Jingchuan Zhou,[4] Erik Swietlicki,[4] and Meinrat O. Andreae[1]

[1] Organic material, about half of which is water soluble, constitutes nearly 80% of the wet-season aerosol mass in the Amazon Basin, while soluble inorganic salts (predominantly ammonium bisulfate) represent about 15%. A detailed analysis of number distributions and the size-dependent chemical composition of the aerosol indicates that, in principle, the sulfate fraction could account for most of the cloud condensation nuclei (CCN) activity. Uncertainty about the chemical speciation of the water-soluble organic component precludes a rigorous analysis of its contribution to nucleation activity. Within reasonable assumptions, we can, however, predict a similar contribution of the organic component to CCN activity as that from sulfate. Because of the nonlinear dependence of droplet nucleation behavior on solute amount, the nucleation activity cannot be attributed uniquely to the inorganic or organic fractions. The role of water-soluble organic compounds as surfactants, however, may be significant (especially in the case of biomass-burning aerosol) and more field measurements are needed to quantify their effects on the surface tension of ambient aerosols. The parametric dependence of the CCN spectra on the physical and chemical properties of the aerosol show that the number distribution, soluble content of the aerosol, and surface tension effects all play an important role in determining CCN spectra. *INDEX TERMS:* 0320 Atmospheric Composition and Structure: Cloud physics and chemistry; 0305 Atmospheric Composition and Structure: Aerosols and particles (0345, 4801); 0365 Atmospheric Composition and Structure: Troposphere—composition and chemistry; *KEYWORDS:* CCN, aerosols, Amazon Basin, composition

1. Introduction

[2] The role of organic material on the nucleating activity of atmospheric aerosols has received much attention in recent years [*Cruz and Pandis*, 1998; *Facchini et al.*, 1999; *Liu et al.*, 1996; *Rivera-Carpio et al.*, 1996]. Measurements of fine aerosol composition have indicated that water-soluble organic species can comprise more than half of the total aerosol mass [*Saxena and Hildemann*, 1996]. Particles smaller than 0.5 μm dry diameter (d_p) account for most of the number concentration; therefore, identifying the physical and chemical properties of aerosol in the cloud condensation nuclei (CCN) size range (i.e., $0.05 < d_p < 0.5$ μm) is important for characterizing CCN spectra.

[3] *Novakov and Penner* [1993] considered their calculations of CCN concentration (N_{CCN}) based on an externally mixed aerosol; yet, they also noted that internally mixed estimations gave the same results within 10%. Although the derivation of N_{CCN} does not critically depend on the assumed mixed state, atmospheric processes do affect the aerosol composition. As an air parcel is likely to be processed through 10 or more nonprecipitating cloud cycles [*Hoppel et al.*, 1990], cloud droplet growth and evaporation modifies the CCN spectrum. A statistical model of CCN growth into cloud droplets suggests that even a low natural variation of supersaturations in cloud processes ($0.3 \pm 0.2\%$ S_v) maintains quasi steady state aerosol number distributions [*Kaufman and Tanré*, 1994] that are similar to those observed over the ocean and Amazon rain forest [*Zhou et al.*, 2002].

[4] Earlier measurements of size-dependent aerosol composition in the Amazon Basin showed that wet-season aerosols in the CCN size range are primarily composed of sulfates and organics [*Artaxo and Hansson*, 1995; *Talbot et al.*, 1990; *Wouters et al.*, 1993]. A large organic component and some sulfate is a characteristic of individual particles, $d_p < 0.5$ μm [*Wouters et al.*, 1993], which supports the observations of significant cloud processing and organic deposition. Biogenic emissions from rain forest vegetation provide a potentially strong source for aerosol formation and growth. The fine-mode

[1]Biogeochemistry Department, Max Planck Institute for Chemistry, Mainz, Germany.
[2]Department of Environmental Engineering, California Institute of Technology, Pasadena, California, USA.
[3]Institute of Physics, University of São Paulo, São Paulo, Brazil.
[4]Department of Physics, University of Lund, Lund, Sweden.

sulfate fraction of Amazonian aerosols may originate to a large extent from the biogenic emissions of reduced sulfur compounds, such as hydrogen sulfide (H_2S) and dimethyl sulfide (DMS) from forest vegetation [*Andreae and Andreae*, 1988; *Andreae et al.*, 1990a]. The fine-mode organic material, which constitutes up to 80% of the aerosol mass [*Artaxo and Hansson*, 1995; *Wouters et al.*, 1993], probably originates from a combination of primary biogenic aerosol and biogenic emissions of volatile organic carbon species (VOCs; i.e., monoterpenes) emitted from forest vegetation. The oxidation products of VOCs yield low and semivolatile compounds that can partition to the aerosol phase. Hence, there may exist a ''cooperative'' relationship between organics and sulfates for aerosol formation, which ultimately influences cloud properties in the Amazon Basin. The sulfate fraction influences CCN properties through addition of soluble material while the organic fraction enhances CCN activity by contributing soluble material and/or lowering the surface tension of a deliquesced aerosol [*Facchini et al.*, 1999; *Shulman et al.*, 1996].

[5] Here, we will discuss results of CCN measurements, in light of the chemical and physical properties of wet-season rain forest aerosol that enable activation and subsequent growth into cloud droplets. Variables that describe the size distribution, soluble content, and surface tension are studied independently to explore the parametric dependence of CCN spectra. Identifying the principal chemical and physical components that define wet-season CCN spectra in the Amazon Basin provides a reference to assess the potential influences of anthropogenic activity, such as biomass burning, on the rain forest climate.

2. Experimental Method

[6] The measurements were performed during the Cooperative LBA Airborne Regional Experiment 1998 (CLAIRE-98), a part of the Large Scale Biosphere-Atmosphere Experiment in Amazonia (LBA). Sampling occurred from 28 March to 15 April 1998, at a ground site (1°55.5′S, 59°24.8′W; 160 m above sea level) located 125 km northeast of Manaus, in the state of Amazonas, Brazil. Isentropic backward air mass trajectories indicate that our site was not affected by anthropogenic sources, including biomass burning. Surface air masses originated from the northeast to east; hence had traveled a thousand kilometers over the most remote regions of the Amazon rain forest for almost a week before being sampled. A total of 185 mm of rain fell during the 19 days of the experiment, which is about normal for the month of April.

[7] We used a static thermal-gradient chamber to determine N_{CCN} at supersaturations (S_v) between 0.15 and 1.5% S_v. Additional aerosol instrumentation, which measured physical and chemical properties and permitted an independent assessment of CCN activity, included a multistage cascade impactor to determine mass distribution ($n_M(D_p)$), a differential mobility particle sizer to measure number distributions ($n_N(d_p)$), and a condensation particle counter to obtain total aerosol concentrations (N). Sampling for each instrument took place 6 m above the ground via individual inlets that were extended 2 m above the roof of

the laboratory. The details of each instrument are discussed in the following sections.

2.1. Static Thermal-Gradient Chamber

[8] CCN measurements were made using a static thermal-gradient diffusion instrument, which operated similarly to the chamber described by *Lala and Jiusto* [1977]. Instead of the original light scattering design, our CCN counter was fitted with a photodiode laser and digital camera to measure droplet concentrations [*Roberts*, 2001]. Activated CCN particles quickly grow to several micrometers in diameter and gravitationally settle out of the chamber. A 670 nm photodiode laser illuminates the activated droplets while the digital camera, normal to the laser beam, registers images every second during the supersaturation cycle. The CCN concentration at a particular supersaturation is determined during post processing. Imaging software (e.g., Image Tools) automatically determines the number of activated CCN in each picture. The CCN concentration is calculated based on the picture with the highest number of particles and on the calibrated illuminated volume. The calibration procedure involved generating a quasi-monodisperse aerosol of a known concentration and counting the number of activated droplets in the digital image. The detection limit is approximately 40 cm^{-3}, which corresponds to 3 droplets in the sample volume. An error analysis indicates that for typical aerosol spectra, the overall measurement error is approximately ±15% at 1.5% S_v and ±30% at 0.15% S_v. These measured analytical errors agree well with theoretical estimates by *Nenes et al.* [2001].

[9] CCN number concentrations were determined every 25 s at a supersaturation between 0.15 and 1.5% S_v (0.15, 0.30, 0.60, 1.0 and 1.5% S_v). CCN spectra were measured every six to seven minutes. A CCN cycle begins with a seven-second flush at 3 liters min^{-1} to remove the previous sample and draw in air for a new sample. The instrument's inlet valve closes and isolates the chamber, which allows the supersaturation profile to develop between two horizontal parallel wetted plates. The CCN counter operates at a desired supersaturation by controlling the temperature difference between the wetted plates. The diameter of the chamber is 100 mm, and the top and bottom plates are separated by 10 mm. The dimensions allow for air in the chamber to reach an equilibrium supersaturation profile in several seconds. Whatman filter papers on the top and bottom plates are kept wetted by an external capillary system. The top plate temperature is allowed to float with the ambient temperature, which ranged from 20 to 35°C, and the bottom plate is cooled as necessary to achieve the prescribed supersaturation. Temperature fluctuations during measurements are usually within 0.1°C, so the supersaturation is constant within ±0.05% S_c.

2.2. Multistage Cascade Impactor

[10] Mass distributions were resolved with a rotating microorifice uniform deposit cascade impactor (MOUDI, MSP Corp.) with 50% cutoff aerodynamic diameters (D_{50}) of 0.093, 0.175, 0.330, 0.560, 1.00, 1.80 and 3.20 μm. The MOUDI impactor uses circular jets on seven impactor stages, plus an eighth inlet stage to remove particles larger than 18 μm. Aerosols were collected on 47 mm diameter Teflon substrates and a quartz-fiber after-filter, which

Table 1. Average Normalized CCN Spectrum During LBA-CLAIRE-98

S_v (%)	$f_{CCN/CN}$					$<D_p>$
	Average	MD_4	MD_6	MD_9	MD_10	nm
0.15	0.070 ± 0.044	0.059 ± 0.033	0.056 ± 0.040	0.063 ± 0.045	0.100 ± 0.060	180
0.30	0.235 ± 0.101	0.228 ± 0.075	0.190 ± 0.085	0.225 ± 0.118	0.297 ± 0.128	130
0.60	0.458 ± 0.152	0.458 ± 0.135	0.396 ± 0.142	0.414 ± 0.154	0.563 ± 0.176	87
1.00	0.682 ± 0.177	0.705 ± 0.153	0.615 ± 0.180	0.618 ± 0.182	0.790 ± 0.194	54
1.50	0.818 ± 0.205	0.824 ± 0.188	0.762 ± 0.201	0.752 ± 0.231	0.935 ± 0.199	41
$N_{1.0}$ (cm^{-3})	265 ± 132	402 ± 102	233 ± 239	206 ± 99	224 ± 89	
Date		3 March to 2 April	4–6 April	9–11 April	11–14 April	
Data recovery	0.86%	0.56	0.91	1.0	0.98	

S_v is the supersaturation of the CCN measurements. $f_{CCN/CN}$ represents the ratio of N_{CCN} to N_{3010} and is determined from a normalized CCN spectrum and $N_{1.5}$ (N_{CCN} at 1.5% S_v). $<D_p>$ shows the number median diameter of Amazonian aerosol at the given supersaturation based on Figure 3a. Concentrations of CCN at 1% S ($N_{1.0}$) are reported in the table. The values in the row titled "data" are the relative time fractions of continuous CCN measurements during the MOUDI sampling. The standard deviations in this paper are reported as one sigma.

collects particles smaller than 0.093 μm; the inlet stage and quartz fiber after-filters were not analyzed. The MOUDI impactor operated at ambient temperature and relative humidity for 48 or 72 hours at an airflow rate of 25–30 liters min^{-1} to collect sufficient particulate mass for analysis. The flow rate was regulated using differential pressure gauges and the volume was measured using a calibrated dry gas meter. The gravimetric analysis was done by weighing each filter before and after sampling with a microbalance (1 μg sensitivity) in a room with stabilized temperature (20°C) and relative humidity (40%). The filters were preequilibrated in this room for at least 24 hours.

[11] Elemental concentrations on each stage of the impactor were analyzed for up to 26 elements using particle-induced X-ray emission analysis (PIXE) at the University of São Paulo, Brazil. Precise experimental details of the PIXE analysis are given elsewhere [*Artaxo and Orsini*, 1987; *Johansson and Campbell*, 1988]. The following 21 elements were detected in the samples: Mg, Al, Si, P, S, Cl, K, Ca, Sc, Ti, V, Cr, Mn, Fe, Ni, Cu, Zn, Br, Sr, Zr, Pb. The detection limit was typically 10 ng m^{-3} for elements with $Z \leq 20$, and around 1 ng m^{-3} for $21 \leq Z < 40$. The precision of the PIXE analysis varied from a few percent for the major elements to about 30% for elements with concentrations near the analytical detection limit.

2.3. Differential Mobility Analysis

[12] The DMPS (Differential Mobility Particle Sizer) has been used to measure the number distribution of aerosol particles with diameters from 0.003 to 0.85 μm [*Zhou et al.*, 2002]. The diameter of the DMPS measurements was accurately determined to within 2% (Zhou, personal communication, 2000). An ultrafine differential mobility analyzer (UDMA) and a differential mobility analyzer (DMA) covered particle diameters from 0.003 to 0.022 μm and 0.022 to 0.85 μm, respectively. The integration of the measured number distribution yields the total aerosol concentration between 0.003 and 0.85 μm. The sheath flow was treated with dryers and the particle size was measured in the dry condition. Individual condensation particle counters (CPC) were used for particle detection after each DMA: ultrafine CPC Model 3025 and CPC Model 7610 (TSI Incorporated, Shoreview, Minnesota, USA). Both CPCs were calibrated for counting efficiency as a function of the particle size. During the measurements, the two DMAs operated in a stepwise scanning mode starting from 0.022 μm diameter, and stepping downward or upwards,

respectively. Equal logarithmic diameter steps were used in the scans for a total of 36 mobility channels. A single scan over the whole size range took 15 min.

[13] The hygroscopic properties of aerosol particles were measured with a H-TDMA (Hygroscopic Tandem Differential Mobility Analyzer) (Zhou et al., submitted manuscript, 2001). The H-TDMA determines, in situ, the hygroscopic diameter growth of individual aerosol particles when taken from a dry state (RH < 10%) to a controlled humidified state. The H-TDMA consists mainly of three parts: (1) a DMA which selects a narrow, quasi-monodisperse size range of the atmospheric aerosol at low RH; (2) humidifiers which condition the air to a well defined RH; (3) and a second DMA which determines the change in diameter caused by the humidification. During the CLAIRE-98 campaign, the H-TDMA measurements were performed for six particle dry diameters (0.035, 0.050, 0.073, 0.109, 0.166 and 0.264 μm) at 90% RH and three dry diameters (0.050, 0.073 and 0.166 μm) at 70% RH. Since CCN activity is estimated from initial dry composition, these growth factors are used to correct the aerodynamic diameters from the MOUDI impactor to equivalent dry aerosol size (section 3.1.1).

2.4. Condensation Particle Counter

[14] An additional CPC Model 3010 (CPC$_{3010}$; TSI Incorporated, Shoreview, Minnesota, USA) measured total ambient aerosol concentrations (N_{3010}) every 30 s and was directly compared to the CCN concentrations to estimate the efficiency of aerosol to serve as CCN. The ratio of the total aerosol concentration (e.g., N_{3010}) to N_{CCN} determines $f_{CCN/CN}$. The CPC$_{3010}$ has a 50% detection efficiency at 0.01 μm and varies from 0 to nearly 100% particle detection from 0.006 to 0.018 μm, respectively. This efficiency curve will be applied in section 3 to compare the measurements of the CPC$_{3010}$ to the aerosol concentration derived from the measured number distribution (N_{DMPS}).

3. Results

[15] CCN number concentrations from the LBA-CLAIRE-98 field experiment were low and resulted in a spectrum resembling those typical of oceanic environments [*Roberts et al.*, 2001]. Table 1 summarizes the mean CCN spectra for the four MOUDI impactor sampling periods. The fractional contribution of N_{CCN} at each supersaturation was normalized to $N_{1.5}$ (at 1.5% S_v) for each supersaturation cycle (e.g., for a given cycle, $N_{0.3}$ was divided by $N_{1.5}$) to exclude bias from

Table 2. Ensemble Average and Standard Deviation (One Sigma) of the Four MOUDI Samples During LBA-CLAIRE-98

Element	Aerodynamic 50% cutoff diameter (D_{50})						
	0.093 μm	0.175 μm	0.33 μm	0.56 μm	1.0 μm	1.8 μm	3.2 μm
Mg	–	–	–	–	2.83 ± 0.91	2.31 ± 0.56	5 ± 1.34
Al	–	–	2.78 ± 0.73	6.72 ± 1.21	17.3 ± 1.8	16.7 ± 1.8	28.3 ± 2.0
Si	2.51 ± 0.66	2.32 ± 0.67	5.98 ± 0.71	12.1 ± 0.8	28.7 ± 1.3	27.1 ± 1.2	30.9 ± 1.3
P	–	–	–	–	1.26 ± 0.2	7.66 ± 0.32	23.4 ± 0.8
S	3.94 ± 0.38	20.6 ± 0.8	20.0 ± 0.8	6.13 ± 0.43	5.64 ± 0.43	7.41 ± 0.47	16.9 ± 0.7
Cl	0.50 ± 0.17	–	–	0.57 ± 0.09	3.37 ± 0.28	11.6 ± 0.5	27.9 ± 1.0
K	–	1.19 ± 0.06	2.18 ± 0.13	1.12 ± 0.09	5.73 ± 0.22	18.3 ± 0.57	53.0 ± 1.6
Ca	–	0.53 ± 0.18	0.17 ± 0.08	0.37 ± 0.08	2.85 ± 0.3	4.17 ± 0.42	6.55 ± 0.46
Sc	–	–	0.05 ± 0.02	0.05 ± 0.01	0.06 ± 0.03	–	–
Ti	–	–	0.18 ± 0.05	0.33 ± 0.06	1.22 ± 0.13	1.5 ± 0.15	3.76 ± 0.25
V	0.04 ± 0.02	–	–	–	–	–	0.06 ± 0.02
Cr	–	–	0.28 ± 0.03	–	–	–	–
Mn	–	–	0.05 ± 0.01	0.03 ± 0.01	0.09 ± 0.01	0.12 ± 0.02	0.21 ± 0.03
Fe	0.19 ± 0.02	0.26 ± 0.05	2.18 ± 0.15	2.87 ± 0.18	7.69 ± 0.42	8.15 ± 0.44	15.2 ± 0.8
Ni	–	–	0.04 ± 0	–	–	–	–
Cu	0.02 ± 0.01	0.03 ± 0.01	0.05 ± 0.01	0.06 ± 0.01	0.07 ± 0.01	0.08 ± 0.01	0.12 ± 0.02
Zn	0.03 ± 0.01	0.04 ± 0.01	0.08 ± 0.01	0.05 ± 0.01	0.09 ± 0.01	0.18 ± 0.02	0.51 ± 0.05
Br	–	–	–	–	–	–	0.2 ± 0.08
Sr	0.02 ± 0.01	0.01 ± 0.00	–	–	0.04 ± 0.01	0.04 ± 0.02	0.07 ± 0.03
Zr	–	0.01 ± 0.00	–	–	0.04 ± 0.01	–	0.05 ± 0.02
Pb	0.01 ± 0.00	0.01 ± 0.00	0.02 ± 0.01	0.01 ± 0.01	0.01 ± 0.01	–	0.02 ± 0.01
mass	96.4 ± 9.6	328.0 ± 32.8	341.5 ± 34.2	262.1 ± 26.2	636.7 ± 63.7	1611 ± 161	4892 ± 489

PIXE and gravimetric analysis determined the elemental and mass concentrations, respectively. Mean elemental aerosol concentrations are reported in ng m^{-3}.

variable absolute concentrations in investigating the shape of CCN spectra. Hence, the standard deviation of $f_{CCN/CN}$, in Table 1, presents the variability of the mean CCN spectrum and not the variability of N_{CCN}. $N_{1.0}$ and the relative time fraction of continuous CCN measurements to the MOUDI sampling period are also reported in Table 1.

[16] Total aerosol concentrations were typically between 300 and 700 cm^{-3} with a mean value of 460 cm^{-3}. Consequently, we find that the average CCN/CN ratios ($f_{CCN/CN}$) also are strikingly high compared to other "continental" measurements, and resemble much more what is conventionally regarded as "marine" values [*Pruppacher and Klett*, 1997]. The high $f_{CCN/CN}$ ratios observed in Amazonia also imply that there are few particles present in the size range below that typical of CCN (i.e., $d_p < 0.05$ μm (at 1.0% S) to 0.10 μm (at 0.3% S) for Amazonian aerosols of mixed composition). The low abundance of aerosol smaller than $d_p = 0.05$ μm has also been confirmed by *Zhou et al.* [2002]. Since small interstitial aerosol particles are representative of recent particle formation, our data also suggest a low rate of new particle formation.

3.1. Physical and Chemical Properties of CCN

[17] A particle's critical supersaturation (S_c) implicitly contains all chemical and dry particle size information and can be calculated for a multicomponent aerosol by separating the dry mass distribution ($n_M(d_p)$) into soluble (i.e., sulfate and/or organic) and insoluble components. The equilibrium saturation ratio (S_v^{eq}) of a droplet of a given diameter (D_p) and temperature (T) is described by a modified Köhler equation as

$$S_v^{eq} = \exp\left(\frac{4\sigma' M_w}{kT\rho_w D_p} - \frac{\Phi M_w}{\frac{\pi \rho' D_p^3}{6} - \sum_i m_i} \left[\sum_i \frac{\nu_i m_i}{M_i} \right] \right) \quad (1)$$

where k is the Boltzmann constant, σ' is the surface tension of the solution, M_w and M_i are the respective molecular weights of water and solute, m_i is the dissolved solute mass, ρ_w and ρ' are the densities of water and aqueous solution, respectively, ν_i is the number of ions into which a solute molecule dissociates (van't Hoff factor), and Φ is the osmotic coefficient of the aqueous solution. The maximum S_v^{eq} of the resulting Köhler curve defines S_c and occurs at the critical droplet diameter (D_{pc}) [*Seinfeld and Pandis*, 1998]. The Kelvin effect (i.e., the surface tension term) accounts for enhanced vapor pressure due to droplet curvature. The Raoult effect (i.e., solute mass term) depresses the vapor pressure due to dissolved mass. Supersaturation ratios are expressed in percent (e.g., S_v (%) = (S_v (ratio) − 1) × 100%) throughout this text.

[18] The following sections apply a closure technique to estimate the CCN activity of rain forest aerosol based on measured $n_M(D_p)$ and $n_N(d_p)$. The independent calculations are compared to the measured results in section 3.2.

3.1.1. Mass Distributions

[19] Four MOUDI impactor samples (e.g., MD_4, MD_6, MD_9 and MD_10), which coincided with CCN measurements, were used for the closure analysis described here. PIXE analysis detected 21 elements and, after converting element concentrations to oxide form, accounted for only 10% of the fine aerosol mass. Table 2 presents the size-resolved chemical composition from PIXE analysis for the ensemble average of the four MOUDI impactor samples. Sulfur was the single most abundant element detectable by PIXE in the fine fraction, but important elements, such as carbon, oxygen and nitrogen, cannot be detected by PIXE. Since these elements constitute a large fraction of the aerosol mass, we have incorporated them into our analysis using approximation from current literature values. Oxide calculations are estimated based on average crustal composition from the following molar ratios: Al_2O_3, CaO,

Table 3. The Soluble (NH_4HSO_4) and Insoluble Inorganic (Oxides) Contribution to the Total Aerosol Mass Collected on Each MOUDI Impactor Stage

Component		Aerodynamic 50% cutoff diameter (D_{50})						
		0.093 μm	0.175 μm	0.33 μm	0.56 μm	1.0 μm	1.8 μm	3.2 μm
Average (ng m^{-3})	mass	96.4 ± 9.6	327 ± 32	341 ± 34	262 ± 26	636 ± 63	1611 ± 161	4891 ± 489
	NH_4HSO_4	14.1 ± 1.4	73.8 ± 2.9	71.8 ± 2.9	22.0 ± 1.6	20.3 ± 1.5	26.6 ± 1.7	60.5 ± 2.6
	oxides	6.2 ± 1.7	7.6 ± 1.8	24.8 ± 3.5	45.8 ± 4.9	128 ± 10	164 ± 10	310 ± 15
MD_4 (ng m^{-3})	mass	179 ± 18	432 ± 43	331 ± 33	280 ± 28	601 ± 60	1209 ± 121	2965 ± 297
	NH_4HSO_4	20.6 ± 1.5	72.7 ± 3.0	63.3 ± 2.6	18.5 ± 1.6	22.0 ± 1.7	25.0 ± 1.7	51.9 ± 2.4
	oxides	4.4 ± 1.5	6.3 ± 1.7	12.7 ± 1.9	36.0 ± 5.6	95.6 ± 10.9	126 ± 10	245 ± 14
MD_6 (ng m^{-3})	mass	57.7 ± 5.8	330 ± 33	314 ± 31	256 ± 26	490 ± 49	1483 ± 148	5232 ± 523
	NH_4HSO_4	9.0 ± 1.4	43.3 ± 2.2	46.7 ± 2.2	8.9 ± 1.2	9.2 ± 1.4	18.5 ± 1.6	52.1 ± 2.4
	oxides	5.6 ± 2.0	3.5 ± 1.5	6.8 ± 1.6	12.2 ± 1.7	44.1 ± 6.1	88.2 ± 7.8	267 ± 15
MD_9 (ng m^{-3})	mass	66.9 ±24.8^a	245 ± 25	354 ± 35	245 ± 25	605 ± 61	1687 ± 169	4978 ± 498
	NH_4HSO_4	13.4 ± 1.3	73.2 ± 2.9	61.8 ± 2.6	17.3 ± 1.5	19.7 ± 1.6	26.8 ± 1.7	55.7 ± 2.5
	oxides	8.6 ± 1.9	9.1 ± 2.1	27.9 ± 5.1	52.9 ± 6.3	136 ± 11	158 ± 9.1	269 ± 14
MD_10 (ng m^{-3})	mass	81.8 ± 8.2	305 ± 31	367 ± 37	268 ± 27	850 ± 85	2065 ± 207	6391 ± 639
	NH_4HSO_4	13.6 ± 1.2	106 ± 4	116 ± 4	43.3 ± 1.9	30.2 ± 1.6	36.2 ± 1.7	82.3 ± 3.0
	oxides	6.4 ± 1.3	11.5 ± 1.7	51.8 ± 5.2	82.2 ± 6.0	240 ± 13	287 ± 14	462 ± 19

These values are used as the mass loading $m_t(D_p)$ for the nonlinear inversion routine discussed in Appendix A.

^{a}Mass and standard deviation (one sigma) for this stage was estimated based on the average ratio of the first and second impactor stages of the other samples.

Fe_3O_4, K_2O, MgO, P_2O_5, SiO_2, TiO_2 [*Mason*, 1966]. These oxides and all other elements except sulfur are considered as the insoluble inorganic component and exhibit an unimodal mass distribution with a median diameter in the coarse size fraction (ca. 3 μm). The gravimetric mass distribution is bimodal with median diameters in the fine and coarse fraction of 0.3 and 4 μm, respectively. Sulfur is also slightly bimodal with the main contribution in the fine aerosol mass fraction and a "tail" that extends into the coarse size fraction. Although no direct measurements of the sulfur speciation have been performed on our samples, earlier aerosol measurements in the Amazon Basin during the wet season show that sulfur is predominantly found as sulfate, SO_4^{2-} [*Gerab et al.*, 1998; *Reid and Hobbs*, 1998]. A stoichiometric balance of the anions and cations [*Gerab et al.*, 1998; *Talbot et al.*, 1990] further indicates that fine particulate SO_4^{2-} has been partially neutralized by ammonium at nearly a 1:1 molar ratio. Therefore, the mass distribution for ammonium bisulfate (NH_4HSO_4) has been estimated using sulfur concentrations from PIXE analysis. The soluble inorganic (e.g., NH_4HSO_4) and insoluble inorganic (e.g., oxides) contribution to the total aerosol mass collected on each impactor stage is shown in Table 3.

[20] Köhler theory (equation (1)) calculates CCN activity based on the soluble content, which lowers a droplet's S_v^{eq} (i.e., Raoult effect). Some of the elements determined by PIXE analysis, such as sulfur (S), chlorine (Cl), potassium (K), and calcium (Ca) could exist as water-soluble anions and cations (i.e., SO_4^{2-}, Cl^-, K^+, Ca^{2+}). Figure 1, however, shows that SO_4^{2-} dominates the inorganic water-soluble fraction for fine aerosol particles. Cl^-, K^+, and Ca^{2+} combined make up less than 5% of the SO_4^{2-} mass and are consequently neglected for the calculation of CCN activity (see section 4). A slightly acidic pH of cloud droplets in the Amazon Basin [*Talbot et al.*, 1990] also inhibits the dissolution of CO_2 to form carbonate anions (CO_3^{2-} and HCO_3^-).

[21] The sampling of nitrates (NO_3^-) in aerosols has long presented experimental challenges; however, several exper-imental and theoretical analyses indicate that, in Amazonia, NO_3^- is predominantly found in the coarse fraction ($d_p > 1$ μm). Single particle analysis of size fractionated aerosol in the Amazon Basin showed that NO_3^- is negligible for aerosol diameters less than 0.5 μm [*Wouters et al.*, 1993]. *Talbot et al.* [1988] and *Artaxo et al.* [1988] found that a maximum of 25% of the total aerosol NO_3^- was contained in the fine fraction and the NO_3^-/SO_4^{2-} fine-mode mass ratio was less than 20%. In addition, theoretical estimations by *Basset and Seinfeld* [1984] have also led to similar conclusions. While SO_4^{2-} and NO_3^- are primarily found in the fine and coarse modes, respectively, the combined fine- and coarse-fraction molar concentrations show that particulate SO_4^{2-} mass tends to be slightly higher than NO_3^- [*Talbot et al.*, 1988, 1990]. Although the variability is large, precipitation chemistry shows similar SO_4^{2-}/NO_3^- mass ratios [*Andreae et al.*, 1990b; *Williams et al.*, 1997]. We believe that NO_3^- in the fine-mode is small compared to SO_4^{2-} (less
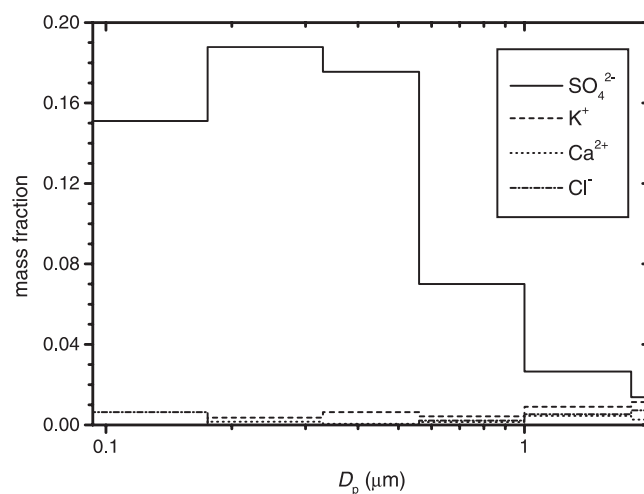

Figure 1. Potential water-soluble anions and cations inferred from elemental concentrations detected in PIXE analysis.

than 20% SO_4^{2-} mass) and can be neglected for CCN activity estimations. Section 4 looks at the errors induced to the mean CCN spectrum by changing the soluble mass—a 20% change in soluble material yields the least significant modification to the mean CCN spectrum of all variables that were studied.

[22] Water-soluble organic carbon compounds (WSOC), such as sugars, sugar derivates, and/or dicarboxylic acids, contribute an undetermined amount of water-soluble species and could induce changes in the droplet's surface tension. Hence, the WSOC component may effect the CCN activity and is analyzed in closer detail in section 3.2.2. The unknown material not detected by PIXE analysis constitutes about 80% of the mass, which is approximately the amount of organic material present in the fine aerosol [*Artaxo and Hansson*, 1995; *Wouters et al.*, 1993; *Mayol-Bracero et al.*, 2002a]. The organic material is estimated from the difference between the total dry mass and the sum of the oxides and NH_4HSO_4 (i.e., the white area below the $n_M(d_p)$ (MOUDI) in Figure 2). Some of this difference could be actually due to remaining adsorbed water, as recent laboratory studies by *McInnes et al.* [1996] have suggested that sea-salt particles on a filter substrate contained 27% water at 40% RH. However, due to the nonhygroscopic nature of the Amazonian aerosol [*Zhou et al.*, 2002], we presume the amount of water retained on the filters is probably less than that, as supported by the estimated mass distributions in Figure 2. Furthermore, in section 4, we show that precise determination of the insoluble inorganic fraction is not critical in estimating CCN activity. The average aerosol mass composition for the fine fraction was ca. 15% NH_4HSO_4, 5% insoluble inorganic, and the other 80% is assumed to be organic material.

[23] The simplest method of reporting MOUDI impactor data is to generate a discrete size distribution from each stage's D_{50}. The aerosol size distribution is assumed to be constant over the range sampled by each stage, and the result looks like a histogram. This method has the advantage of simply and unambiguously representing the raw data. However, the histogram representation is inappropriate for the calculation of CCN activity. A continuous mass distribution of important constituents (i.e., soluble and insoluble material) is necessary to compute CCN spectra. The mass collected on each stage (Table 3) was used to derive the continuous mass distributions (Figure 2) for each of the MOUDI impactor sample periods. The basis of our inversion technique used an adaptation to the Twomey nonlinear iterative algorithm that is described by *Winklmayr et al.* [1990], referred to as WWJ90 hereafter. Several important modifications have been made to the WWJ90 inversion technique and are outlined in Appendix A. Extrapolating the composition to aerosol sizes smaller than the D_{50} of the lowest MOUDI impactor stage (i.e., $D_p < 0.093$ μm) introduces significant error for estimations at supersaturations > 0.6% S_v.

[24] The mass distributions in Figure 2 have been calculated to dry aerosol diameters based on hygroscopic growth factor measurements. The MOUDI impactor separates the aerosol according to their moist aerodynamic diameter, which is influenced by the diel changes in relative humidity (RH). The DMPS, however, measures number distributions by dry electrical mobility diameters. Therefore, to deter-mine the chemical composition at a dry diameter, the aerodynamic diameter in the inverted distribution needs to be corrected to account for hygroscopic growth. H-TDMA growth factor measurements (Table 4) were obtained at 90% RH and may not necessarily reflect the actual growth factor for the MOUDI impactor, because of the wide range of relative humidity (i.e., between 40 and 100% RH) throughout the sampling period. Hence, a hygroscopic growth model [*Swietlicki et al.*, 1999] was used to estimate mean growth factors, which were weighted by ambient relative humidity to account for nonlinearity in hygroscopic growth. These weighted growth factors are also summarized in Table 4. Hygroscopic growth is less for smaller particles because of the increased influence of the Kelvin effect. A power law relationship between dry particle diameter and weighted hygroscopic growth converts the mass distribution from aerodynamic wet diameters to dry diameters.

[25] The MOUDI impactor provides the necessary chemical information to determine a particle's critical supersaturation (S_c) at given diameter using Köhler theory. However, deriving the number concentration from the mass distribution can yield unreliable results due to the r-cubed dependence and the variation in growth factors from changing relative humidity. In addition, the size cutoffs in the MOUDI impactor vary by a factor of 2 between stages. The DMPS measurements, on the other hand, accurately determined the aerosol number concentrations as a function of size. A dry particle density of 1.5 g cm^{-3} was used in deriving the mass distribution from the DMPS measurements (Figure 2). Hence, the measured number distribution of the DMPS, combined with the relative chemical information of the MOUDI, provides a reliable estimate of CCN spectra.

3.1.2. Number Distributions

[26] The number distributions measured by the DMPS were averaged to determine the mean distribution for the corresponding MOUDI impactor sampling period (Figure 3). Both Aitken (0.02 < d_p < 0.1 μm) and accumulation (0.1 < d_p < 1 μm) modes were present with the median diameters 0.068 and 0.15 μm, respectively. A nucleation mode (d_p < 0.02 μm) was rarely observed and there is a strong indication that ultrafine particles were not formed close to the ground, but most likely aloft [*Zhou et al.*, 2002]. Airborne measurements in the Amazon Basin have found evidence that new particle formation may occur near cloud boundaries (Roberts et al., Airborne measurements of CCN in the Amazon Basin, manuscript in preparation, 2001). The accumulation mode particles may have been formed via in-cloud processing of Aitken mode particles through the uptake of SO_2 in heterogeneous reactions in cloud droplets [*Bower and Choularton*, 1993; *O'Dowd et al.*, 1999].

[27] The total aerosol concentrations estimated by integrating the 36 DMPS measuring channels (0.003 < d_p < 0.85 μm) were compared to CPC_{3010} measurements. Since the number distribution includes particles below the detection limit of the CPC_{3010}, the efficiency curve of the CPC_{3010} (section 2.4) was utilized when calculating the DMPS-derived aerosol concentration, N_{DMPS}. The CCN spectra closure (section 3.2) uses N_{DMPS} to determine the theoretical fraction of CCN to total aerosol concentration. N_{DMPS} were slightly higher than N_{3010} with a regression
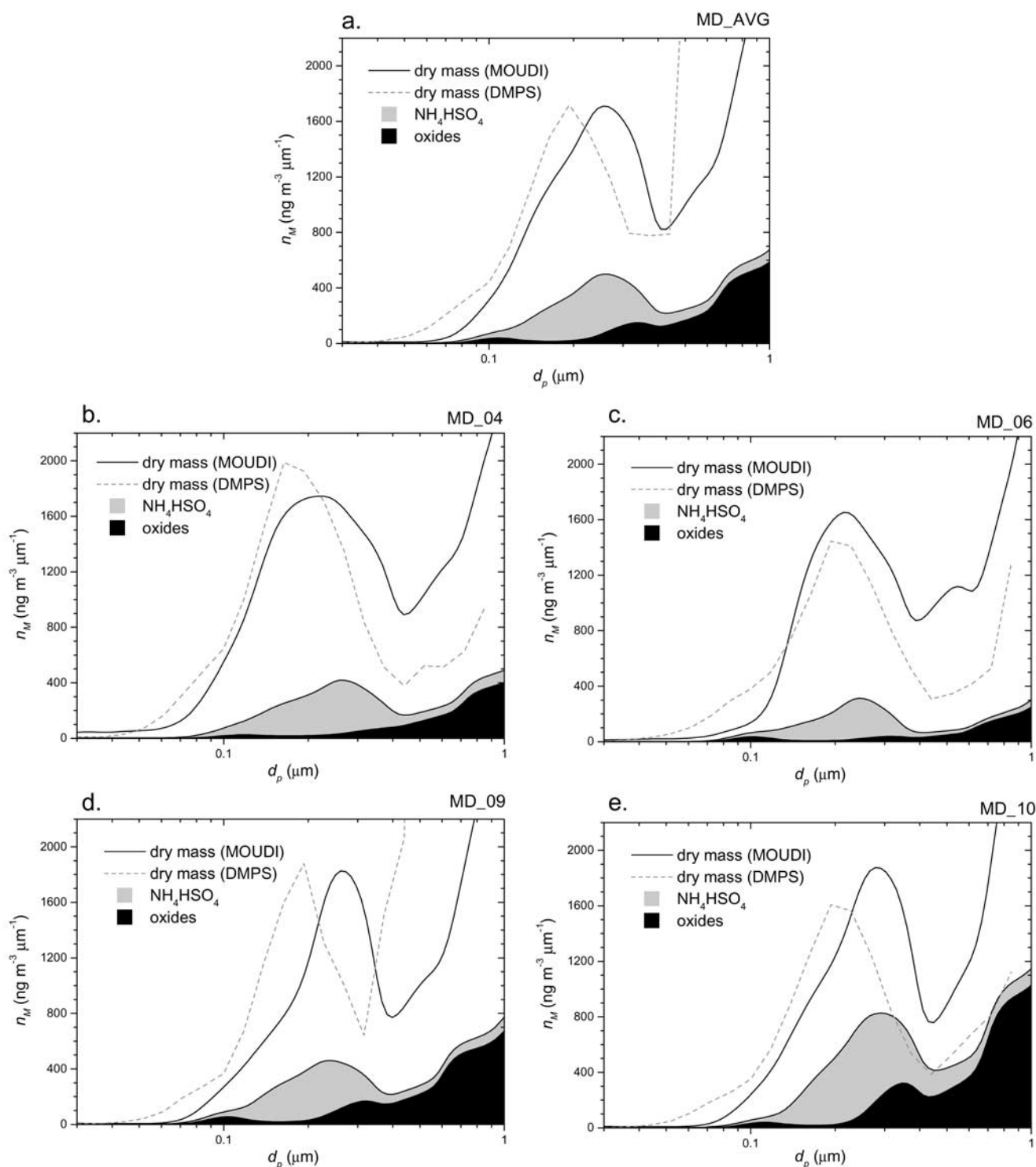
Figure 2. Inverted $n_M(d_p)$ (dM dlog$^{-1}d_p$) of MOUDI impactor data. Total dry aerosol mass was determined gravimetrically. NH$_4$HSO$_4$ and oxides were calculated based on PIXE analysis for S and average crustal composition (i.e., Al$_2$O$_3$, SiO$_2$, etc...), respectively. The remaining material (white area under $n_M(d_p$, dry mass)) has not been identified and is probably organic matter. RH growth factors from Table 4. Mass distributions derived from DMPS measurements (ρ = 1.5 g cm^{-3}) are shown for comparison.

Table 4. Summary of Aerosol Hygroscopic Properties During the LBA-CLAIRE 1998 Experiment

	d_p					
	0.035 μm	0.050 μm	0.073 μm	0.109 μm	0.166 μm	0.264 μm
Growth factor[a]	1.17 ± 0.05	1.16 ± 0.04	1.17 ± 0.04	1.22 ± 0.06	1.26 ± 0.07	1.32 ± 0.07
Soluble fraction[b]	0.20 ± 0.06	0.17 ± 0.05	0.16 ± 0.05	0.21 ± 0.07	0.24 ± 0.08	0.31 ± 0.09
MD_04[c]	1.18 ± 0.09	1.18 ± 0.10	1.19 ± 0.12	1.26 ± 0.17	1.32 ± 0.22	1.40 ± 0.29
MD_06[c]	1.23 ± 0.08	1.24 ± 0.10	1.26 ± 0.13	1.36 ± 0.19	1.45 ± 0.25	1.57 ± 0.33
MD_09[c]	1.24 ± 0.07	1.25 ± 0.09	1.27 ± 0.1	1.37 ± 0.15	1.45 ± 0.19	1.57 ± 0.25
MD_10[c]	1.19 ± 0.08	1.19 ± 0.09	1.2 ± 0.1	1.27 ± 0.15	1.33 ± 0.19	1.42 ± 0.24

[a] Growth factor measured at 90% RH [*Zhou et al.*, 2002].
[b] Soluble mass fraction based on a NH_4HSO_4 and inactive core aerosol [*Zhou et al.*, 2002].
[c] Growth factor weighted by diel changes in RH [*Swietlicki et al.*, 1999].

slope of 1.10 ($r^2 \approx 0.91$) [*Zhou et al.*, 2002]. The discrepancy is likely due to different sampling inlets and/or inlet losses from the low sample flow of the CPC_{3010}.

3.2. CCN Spectra Closure

[28] The results of the mass (Figure 2) and number (Figure 3) distributions, which have been described in section 3.1 enable independent calculations of CCN spectra and will be compared to the measured CCN spectra reported in Table 1. A multiple-component approach allows for a closer approximation of CCN activity as the water soluble and insoluble components are comprised of both inorganic and organic material and can be treated as such in the Köhler equation (equation (1)). The ratio of each component (i.e., soluble/insoluble inorganic/organic material) is estimated using the mass distributions from Figure 2 to determine the relative contribution of soluble and insoluble components. Chemical and physical properties of each component that dictate a particle's S_c are shown in Table 5. Integrating the number distribution above a given diameter, which exhibits a particular S_c, yields N_{CCN} at that supersaturation. Furthermore, $f_{CCN/CN}$ can be determined by the ratio of the calculated N_{CCN} to N_{DMPS} and compared to measured values shown in Table 1.

3.2.1. Three-Component CCN Spectra

[29] Using the measurements presented in section 3.1, the simplest approach for estimating CCN spectra divides the aerosol mass into three components—soluble inorganic (NH_4HSO_4), insoluble inorganic (oxides), and insoluble organic (the unknown mass) as shown in Figure 2. The critical supersaturation, calculated by equation (1) and the aerosol properties in Table 5, varies with composition, but generally decreases with increasing diameter. The resulting relationships between S_c and D_p are shown in Figure 3. Figure 3 also shows limiting cases for pure NH_4HSO_4 and insoluble aerosol to illustrate the maximum range of S_c. The relationships between a particle's S_c and d_p are combined with the number distribution, also shown in Figure 3, to yield the independent calculations of CCN spectra (Figure 4). Integration of $n_N(d_p)$ until a dry particle's S_c equals S_v of the CCN instrument, results in a theoretical N_{CCN}. For example, a particle of $d_p = 0.054$ μm has a critical supersaturation of 1.0% S_v based on the three-component model (Figure 2a). Therefore, the area under $n_N(d_p)$ in Figure 3a from $0.054 < d_p < 0.850$ μm is the concentration of aerosol expected to activate at 1.0% S_v in the CCN counter. The computed N_{CCN} is divided by the total aerosol concentration, N_{DMPS}, to calculate $f_{CCN/CN}$. The resulting

CCN spectra (Figure 4), which utilize a simplified three-component model of NH_4HSO_4 and insoluble constituents, agree particularly well with the measured results reported in Table 1.

[30] Estimates for the H-TDMA-derived soluble mass fraction in Table 4 [*Zhou et al.*, 2002] provide a third independent method of calculating CCN spectra (section 3.2.1). *Zhou et al.* [2002] concluded that ca. 20% of the aerosol mass fraction from $0.03 < d_p < 0.26$ μm was soluble (Table 4) based on calculations of a bicomponent aerosol (i.e., NH_4HSO_4 and an insoluble core). The density of the insoluble core was assumed to be 1.5 g cm^{-3}. A CCN spectrum, generated from the H-TDMA results, is shown in Figure 5, along with the CCN spectrum based on the MOUDI composition for comparison. The CCN spectra were generated from the average number distribution (Figure 2a). As the soluble component from the H-TDMA measurements is similar to that determined by the MOUDI impactor, the resulting CCN spectra agree quite well.

3.2.2. Four-Component CCN Spectra
3.2.2.1. Organic Component: Solute Effect

[31] Aerosol in the Amazon Basin has a large organic component, and about half of which is water soluble. However, uncertainty about the chemical speciation and the solubility of WSOC precludes a rigorous analysis of its contribution to nucleation activity. Within reasonable assumptions about molecular weight, density and van't Hoff factor, we can predict a similar contribution to CCN activity as that from the soluble inorganic component. Figure 6 shows the potential contribution of 40% aerosol mass of completely soluble WSOC to the CCN spectra. To illustrate the differences in CCN activity based on molecular weight, WSOC are divided into smaller compounds (e.g., dicarboxylic acids (DCA); 140 g mol^{-1}) and humics (1400 g mol^{-1}). The contributions of 40% mass of completely soluble DCA and humics are separately shown in Figure 6. An increase in molecular weight reduces the solute effect term (i.e., Raoult term) and, subsequently, reduces CCN activity. Surface tension effects are not included in Figure 6 and will be discussed in the next section.

[32] The combined contribution of 15% NH_4HSO_4 and 40% completely soluble WSOC (i.e., DCA), shown in Figure 6, overestimates the solubility effects consistent with our measurements. Completely soluble WSOC probably exaggerates the solubility of ambient aerosol WSOC, but serves to illustrate the maximum contribution of WSOC to CCN activity. Presumably, ambient aerosol would contain a
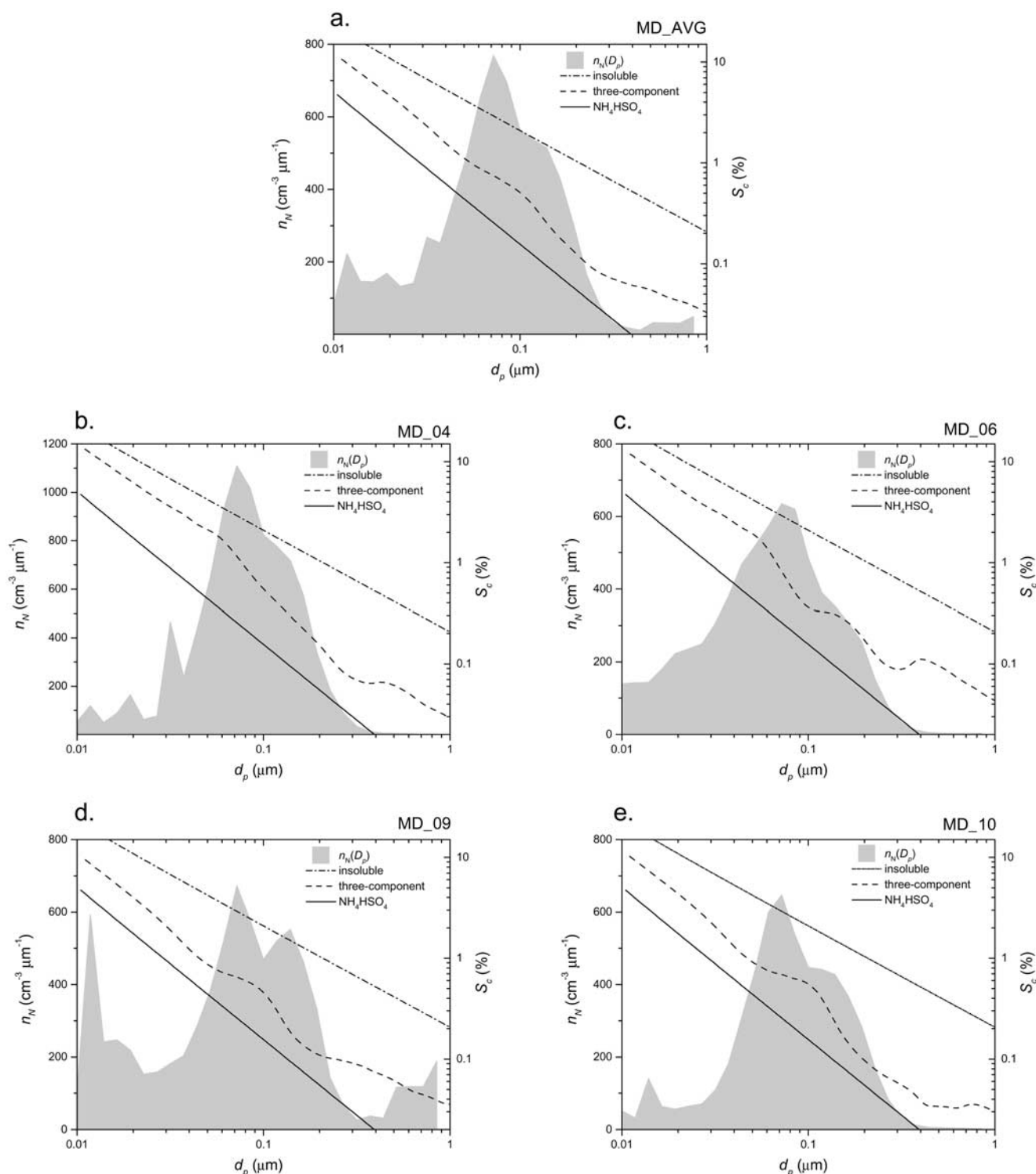
Figure 3. Number distributions ($dN \, dlog^{-1} d_p$), averaged for the respective MOUDI sample, are shown in gray. S_c was calculated for the three-component model using the chemical composition shown in Figure 2. Limiting cases for S_c are represented by pure NH_4HSO_4 and insoluble aerosol.

mix of sulfate, DCA and humics—at mass ratios and solubility that provide a good match to the observations. Because of the nonlinear dependence of droplet nucleation behavior on solute amount (sections 4 and 5; Figure 10), the nucleation activity cannot be attributed uniquely to the inorganic or organic fractions. For example, an initially

organic aerosol could readily activate into a cloud droplet due to a relatively small amount of WSOC. The subsequent acquisition of sulfate from cloud processing [*Bower and Choularton*, 1993; *O'Dowd et al.*, 1999] would then enhance CCN activity. However, the addition of sulfate will not increase CCN activity in a linear fashion. The opposite

Table 5. Properties of Important Components Used in Köhler Theory to Estimate CCN Activity

Material	Density (g cm^{-3})	Molecular weight (g mol^{-1})	Solubility (mole liter^{-1} H$_2$O)	van't Hoff factor
NH$_4$HSO$_4$	1.780[a]	115.11[a]	6.55[a]	2.0
WSOC	1.3[b]	140[b]	0.1–0.001 (carbon)[c]	1.0
Insoluble inorganic	2.5[d]	NA	0.0	0.0
Insoluble organic	1.3[b]	NA	0.0	0.0

[a] *CRC Handbook* [*Lide*, 2000].
[b] Values are similar to WSOC such as glutaric and adipic acid.
[c] *Facchini et al.* [1999].
[d] Average crustal material [*Mason*, 1966].

scenario would also be true for particles that initially contain inorganic salts and accumulate WSOC by partitioning of semivolatile organic compounds [*Kavouras et al.*, 1998].

3.2.2.2. Organic Component: Surface Tension Effect

[33] Nonidealities, such as the interactions of alkaline ions on WSOC and the subsequent effects on σ', are difficult to assess. *Shulman et al.* [1996] and *Facchini et al.* [1999] determined the relationship between dissolved WSOC concentrations and the reduction in surface tension for specific WSOC and bulk atmospheric cloud water samples, respectively. Both studies show similar changes in surface tension. However, as detailed chemical analysis of the organic fraction has not been performed, Facchini's relationship was applied here to estimate potential influences of surfactants on wet-season CCN spectra in the Amazon Basin. *Facchini et al.* [1999] determined the relationship of σ' as a function of dissolved organic carbon (DOC) concentration for fog and cloud water samples. DOC concentrations ($10^{-4}-10^{-2}$ M) that exist for droplet sizes near D_{pc} were recreated by evaporating the fog or cloud liquid sample volumes up to several orders of magnitude. The change in surface tension ($\Delta\sigma'/\sigma'$) was measured revealing a -30% $\Delta\sigma'/\sigma'$ at the highest concentration (i.e., 10^{-1} M DOC). DOC concentrations less than 0.001 M exert minor changes to the droplet surface tension and the soluble effect is negligible. A range of WSOC from 0.001 to 0.1 M DOC will be applied here to estimate potential influences of surfactants on wet-season CCN spectra in the Amazon Basin by adding a fourth component to the multicomponent model.

[34] The organic component, which constitutes nearly 80% of the aerosol mass, can be separated into soluble and insoluble terms. As in the earlier section, the WSOC content is estimated as 50% of the total organic composition. Changes in surface tension are estimated based on the relationship described by *Facchini et al.* [1999] for 0.001, 0.01 and 0.1 M DOC and corresponds to $\Delta\sigma'/\sigma'$ of -3.8, -15 and -30%, respectively. The modifications to the CCN spectra in Figure 7 result from the combined effects of surface tension and DOC solubility on CCN spectra. Changes in σ' influence CCN activity more than WSOC solubility (see section 4), and -15% $\Delta\sigma'/\sigma'$ is probably the upper limit of the surface tension effects consistent with our measurements in the Amazon Basin (Figure 7).

4. Quantifying the Sensitivity of CCN Spectra

[35] The number distribution, soluble content of the aerosol, and surface tension effects all play an important role in determining CCN spectra and each of these factors were incorporated in the analysis in section 3. However, their individual contribution in regulating CCN spectra is not known and will be quantified in this section. Studying the effects of the individual components that influence CCN spectra allows us to identify the most important aerosol properties that determine CCN activity.

4.1. Key Parameters

[36] Idealized size distributions with prescribed $n_N(d_p)$ and chemical composition are used to clearly sort out the physics involved. Number distributions are of the single-mode lognormal form

$$\frac{dN}{d\log d_p} = \frac{N}{\sqrt{2\pi}\ln\sigma_g}\exp\left[\frac{-(\ln d_p - \ln d_{pg})^2}{2\ln^2\sigma_g}\right] \quad (2)$$

where N is the aerosol number concentration, d_{pg} is the number mode diameter, and σ_g is the geometric standard deviation. Values for N, d_{pg} and σ_g that best represent the average wet-season number distribution are 459 cm^{-3}, 0.0823 μm, and 1.83, respectively. A particle's S_c is determined for a three-component aerosol using the measured averages (e.g., 15% NH$_4$HSO$_4$, 5% insoluble inorganic, 80% insoluble organic; section 3.2.1) and is uniform for all d_p. These physical and chemical properties establish a size distribution that yields a reference CCN spectrum.

4.2. Parametric Dependence

[37] To explore the parametric dependence of CCN spectra, variables that describe the size distribution, soluble content, and surface tension were independently studied (Figure 8). The modifications to the reference CCN spectrum were quantified for a given supersaturation from the following expression:

$$\delta_S = |N_\Delta - N_S| \quad (3)$$

where N_S and N_Δ are the CCN number concentrations for the reference and modified CCN spectra, respectively, and δ_S describes the absolute difference at a given supersaturation. Table 6 summarizes the change in CCN spectra for $S_v < 1.5\%$ for a 20% change in physical and chemical parameters that influence CCN activity based on the initial conditions stated in the previous section. Figure 9 presents δ_s as a function of S_c to easily compare the parametric modifications, which are discussed in more detail below.

[38] The number distribution, approximated by a lognormal function (equation (2)), depends on three parameters (i.e., N, D_{pg} and σ_g), that are individually investigated.
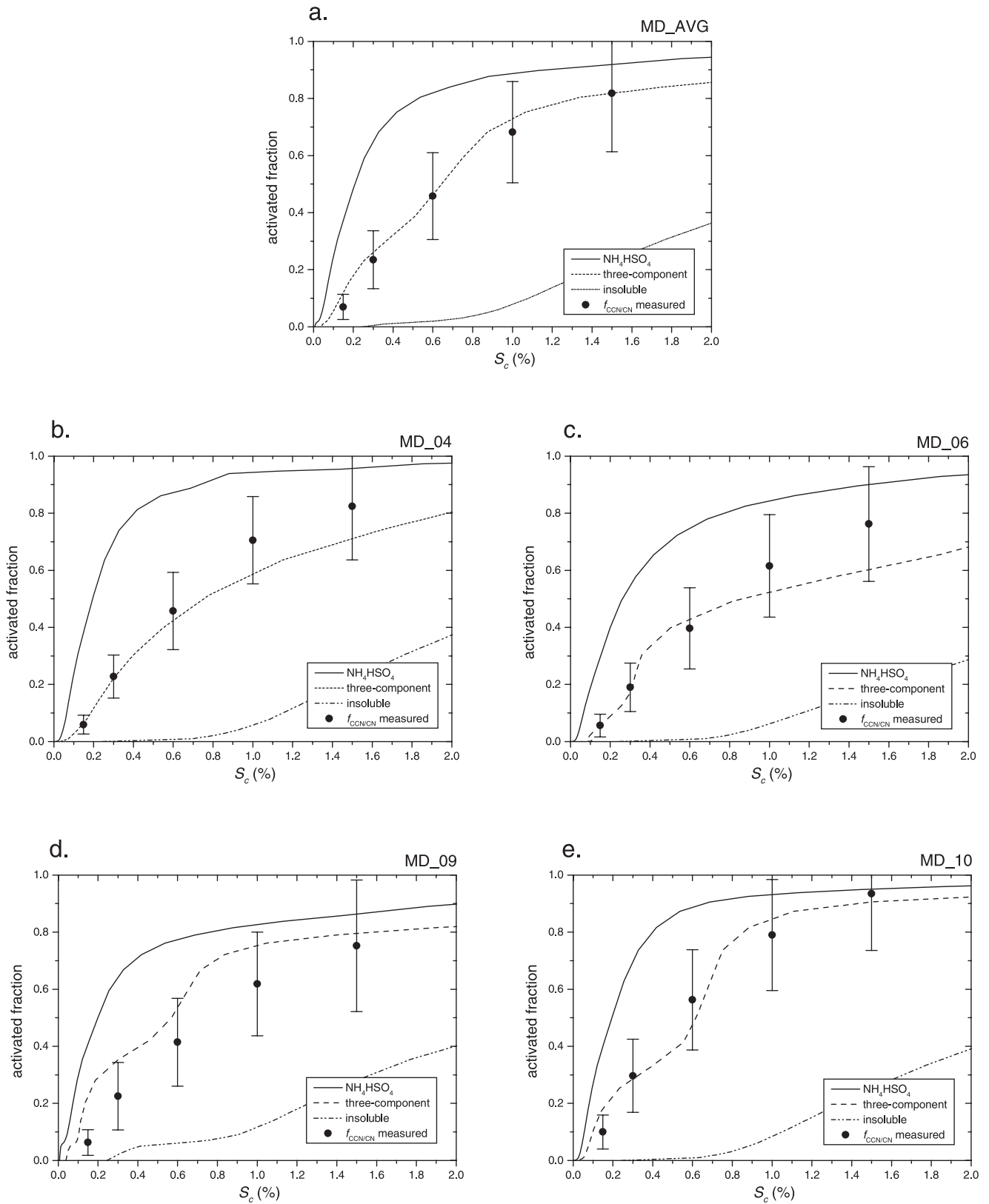
Figure 4. Fraction of aerosol expected to activate as CCN for a three-component model. The spectra were calculated using the relationship between $n_M(d_p)$ and S_c shown in Figure 3. Examples of pure NH_4HSO_4 and insoluble aerosol illustrate the limiting CCN spectra.
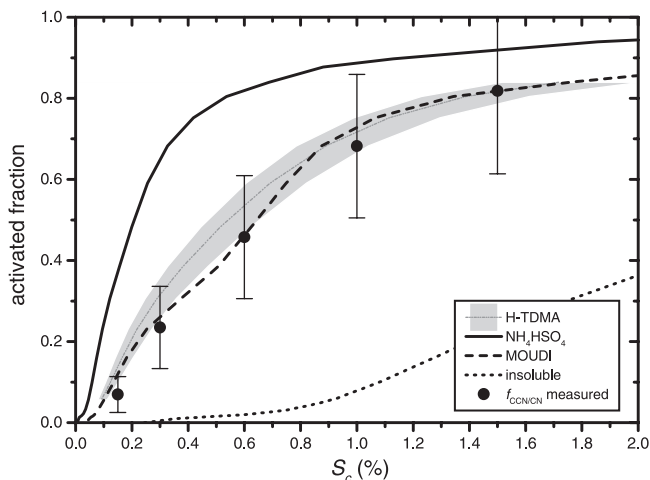
Figure 5. Average CCN spectra for MOUDI and H-TDMA soluble fractions of NH_4HSO_4. The gray area indicates the error in the spectra for the DMPS calculations.

Figure 7. Effect of surface tension on CCN spectra. The change in surface tension $\Delta\sigma'/\sigma'$ was estimated using the relationship described by *Facchini et al.* [1999]. WSOC concentration of 0.1, 0.01, and 0.001 M DOC corresponded to $\Delta\sigma'/\sigma'$ of −3.8, −15 and −30%, respectively. Pure NH_4HSO_4 and insoluble aerosol represent the limiting cases.

1. An increase or decrease in N directly affects the number of CCN available for activation and shifts CCN spectra accordingly (Figure 8a).

2. The geometric median diameter (d_{pg}) affects CCN spectra (Figure 8b) by dictating the fraction of aerosol larger than a critical dry diameter (d_{pc}), which is the smallest diameter that will activate at a given supersaturation. Increasing or decreasing d_{pg} results in respective changes to the activated aerosol fraction, $f_{CCN/CN}$. When $d_{pg} > d_{pc}$, a 20% decrease in d_{pg} has a greater effect on CCN spectra because the higher "shoulder" of the number distribution extends to sizes smaller than d_{pc}. Note: the opposite would be true when $d_{pg} < d_{pc}$.

3. The geometric standard deviation (σ_g) affects the shape of the number distribution. Increasing σ_g flattens $n_N(d_p)$ by

reducing the peak height and extending $n_N(d_p)$ over a larger size range. Since larger aerosol sizes correspond to smaller S_c, particles initially activate at lower S_c and increase N_{CCN} (i.e., raise the CCN spectrum; Figure 8c). The CCN concentrations for the reference and modified CCN spectra are equal when $d_p = d_{pg}$. This occurs at the critical supersaturation of d_{pg}. At larger critical supersaturations (i.e., $d_p < d_{pg}$), fewer CCN activate because particles extend to smaller sizes when σ_g increases. Conversely, reducing σ_g sharpens $n_N(d_p)$ and reduces the number of CCN available for activation at low supersaturations, resulting in an initial reduction in CCN spectra. Furthermore, the CCN concentration increases when $d_p < d_{pg}$ because of the narrower number distribution. A 20% decrease in σ_g has a larger effect on CCN spectra than a similar increase in σ_g and 20% changes in the water soluble content.

[39] The effects of water-soluble content on CCN spectra have been used throughout this paper to illustrate the limiting cases of completely soluble and insoluble particles. In this discussion, we consider a 20% change to the NH_4HSO_4 mass fraction to quantify the effects of the soluble fraction (Figure 8d). The interpretation of these modifications is not restricted to NH_4HSO_4 and may be applied to any water-soluble species, including WSOCs. A particle's S_c is inversely proportional to its water-soluble content. Hence, increasing or decreasing the water-soluble content enhances or reduces CCN spectra, respectively. A 20% change in NH_4HSO_4 (i.e., soluble material) yields the least change to CCN spectra (Table 6). The changes, however, are not linear and Figure 10 illustrates that modifications to CCN spectra are most sensitive at lower S_c. Therefore, a reduction in the soluble fraction exerts a greater impact on resulting CCN spectra than an increase. Furthermore, a 20% change of soluble material is more important for aerosols that initially contain less soluble material.
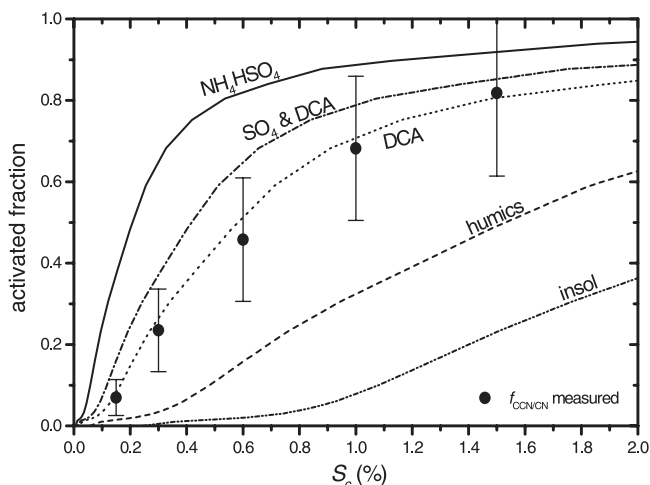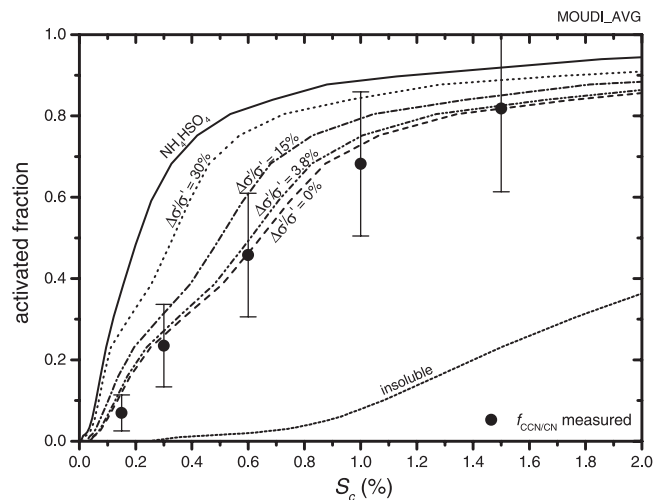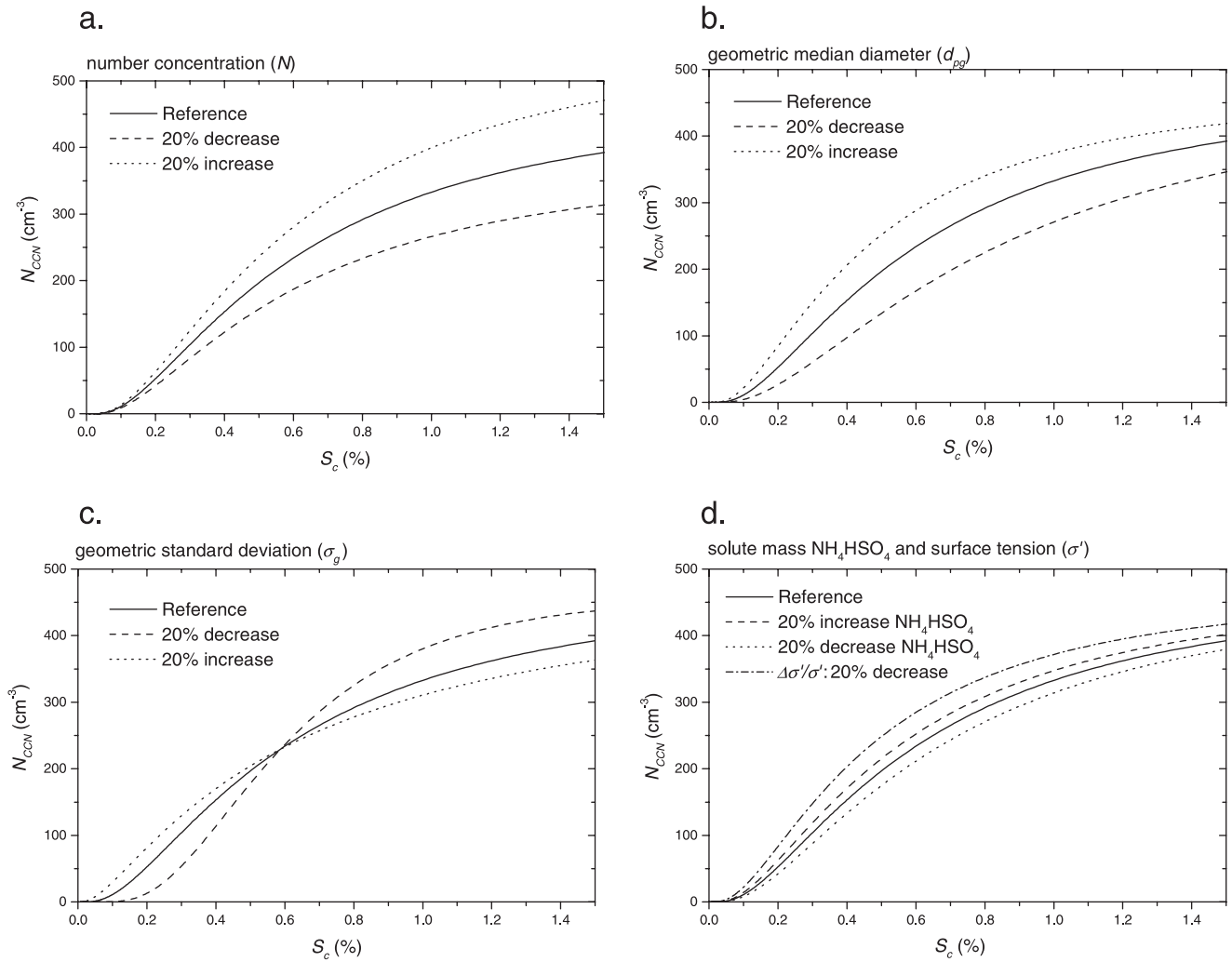

Figure 6. Potential effect of completely soluble WSOC on CCN spectra. The CCN spectra for a 40% soluble mass are labeled separately for dicarboxylic acid (DCA) (140 g mol^{-1}) and humic substances (1400 g mol^{-1}). "SO4 & DCA" shows the combined contribution of NH_4HSO_4 and DCA. Pure NH_4HSO_4 and insoluble aerosol represent the limiting cases.

a.

number concentration (N)

b.

geometric median diameter (d_{pg})

c.

geometric standard deviation (σ_g)

d.

solute mass NH$_4$HSO$_4$ and surface tension (σ')

Figure 8. Modification in the reference CCN spectra due to changes in physical and chemical properties that affect CCN activity.
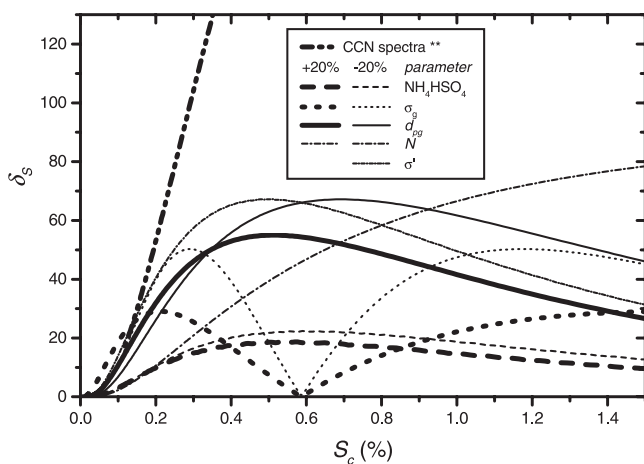

Figure 9. Sensitivity of CCN spectra on parameters that influence a particle's S_c. ****Reference CCN spectra compared to insoluble CCN spectra—measures the effect of 15% addition of NH$_4$HSO$_4$.

[40] Lowering a droplet's σ' changes droplet growth characteristics and is another parameter that needs to be explored. A 20% decrease in σ' yields a reduction in CCN spectra (Figure 8d) that is similar to modifications in parameters that describe the number distribution (e.g., D_{pg}, σ_g and N). An increase in surface tension is not physically relevant and is not included in our analysis.

[41] Quantifying the average modification in CCN spectra depends on the range of supersaturation; however, the general trends remain the same. The average absolute difference $\langle\delta_S\rangle$, reported in Table 6, were calculated for <1.5% S_v. Parameters that dictate the number distribution and surface tension effects are relatively more important than varying the soluble content. The role of WSOCs as surfactants may be significant, especially for biomass-burning aerosol, and more field measurements are needed to quantify the effects of surface tension on ambient aerosols.

5. Discussion

[42] As the timescales of our closure estimation are determined by the sampling time of the MOUDI impactor,

Table 6. Parametric Changes That Effect the CCN Spectra

Parameter	$\langle\delta_S\rangle$
20% mass increase of NH_4HSO_4 (12% NH_4HSO_4, 5% insoluble inorganic, 83% insoluble organic)	13.4
20% mass decrease of NH_4HSO_4 (18% NH_4HSO_4, 5% insoluble inorganic, 77% insoluble organic)	16.4
20% increase in lognormal standard deviation ($\sigma = 2.20$)	19.0
20% decrease in lognormal standard deviation ($\sigma = 1.46$)	35.2
20% increase in median diameter ($D_{pg} = 0.0999$ μm)	39.1
20% decrease in surface tension ($\sigma = 57.07$ dyne cm^{-1})	47.3
20% increase/decrease in number concentration ($N = 367$ and 550 cm^{-3})	48.6
20% decrease in median diameter ($D_{pg} = 0.0666$ μm)	50.8
insoluble CCN spectra compared to reference CCN spectra—measures the effect of 15% addition of NH_4HSO_4	235.8

$\langle\delta_S\rangle$ shows the average absolute change in the CCN spectrum for $S_v < 1.5\%$. The parameters that effect the CCN spectra are listed from least important to most important factors.

the natural variability of CCN spectra over a two-day period limits the resolution at which the chemical influences can be discerned. Nevertheless, our results suggest that, while the soluble inorganic component contributes relatively little to the total aerosol mass, ca. 15% NH_4HSO_4 is sufficient to account for the observed CCN activity during the wet season in the Amazon Basin. However, the change in CCN spectra is not linear with soluble fraction. Figure 10 illustrates the changes in CCN spectra based on the three-component model for various amounts of NH_4HSO_4. We use NH_4HSO_4 for comparison to our measured results; yet, the same trend would be observed for any water-soluble compound of similar molecular weight. The average number distribution (Figure 3a) was used to derive CCN concentrations for Figure 10. CCN spectra are most sensi-

Figure 10. CCN spectra for a three-component model of various amounts of NH_4HSO_4. The spectra were calculated using the average number distribution (Figure 4a). The insoluble inorganic mass contribution was 5%; while the insoluble organic contribution depended on the NH_4HSO_4 mass fraction.

tive at the low solute amount case, where even a 5% contribution of water-soluble material is enough to raise the CCN spectrum by an amount detectable within the measurement errors. The difference between CCN spectra of 50% and 100% water-soluble matter material, however, is significantly less than the change for the low solute amount case. This apparent insensitivity to a notable increase in soluble material was highlighted in Figure 6 by combining solute effects of NH_4HSO_4 and WSOC. Although the results from the earlier section indicate that varying the soluble content induces relatively small changes to the reference CCN spectrum, the difference between the reference CCN spectrum and the insoluble CCN spectrum is much greater than any other modification (Figure 9). Therefore, the existing presence of soluble compounds in the aerosol reduces the sensitivity of CCN spectra to the contribution of moderate additional amounts of other water-soluble species.

[43] Although organic material constitutes nearly 80% of the aerosol mass in the Amazon Basin [*Artaxo and Maenhaut*, 1990; *Wouters et al.*, 1993], its effect on CCN activity of wet-season aerosol cannot be readily determined from our CCN measurements. Since the water-soluble inorganic fraction of the fine-mode aerosol is primarily sulfate, we hypothesize that even a small mass fraction of sulfate present on a particle plays a significant role in dictating CCN activity. This hypothesis, however, does not suggest that organic compounds cannot serve as CCN. Organic compounds cover a very wide range of molecular forms, solubilities, and physical properties, which makes a complete characterization extremely difficult. Since a large fraction of the biomass-burning aerosol consists of humic-like substances [*Mayol-Bracero et al.*, 2002b], the solubility and surface tension effects of biomass-burning aerosol may play an important role in increasing the CCN activity during the dry season. *Novakov and Corrigan* [1996] report that pure organic smoke from cellulose is able to form CCN without being associated to sulfates or other inorganic compounds. Based on their reported size distribution and activated CCN fractions, a ca. 5–10% soluble mass fraction can account for their measured CCN activity. Levoglucosan,
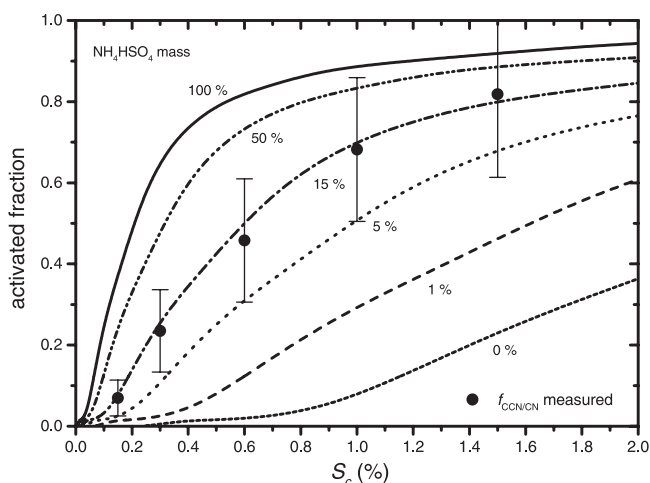
a highly soluble anhydro-sugar present in biomass-burning smoke [*Graham et al.*, 2002], or soluble humic-like compounds [*Mayol-Bracero et al.*, 2002b] could exist in sufficient quantities to account for CCN activity in the absence of soluble inorganic salts. Less than ca. 5% soluble mass fraction may also be possible when considering surface tension effects. However, surface tension effects alone probably do not account for CCN activity as $\Delta\sigma'/\sigma'$ would need to be at least -50% to reproduce the observed CCN activity reported by *Novakov and Corrigan* [1996]. Such a reduction in σ' is tenuous based on the measurements by *Facchini et al.* [1999, 2000].

[44] These results present challenges for both the experimental and modeling communities. In order to measure the effects of organic material in ambient aerosols, the precision of CCN measurements will have to be improved. The required precision of CCN measurements depends largely on the sensitivity of cloud properties to variations in the CCN spectrum from modeling studies. *Facchini et al.* [1999] estimated a 6% decrease in effective cloud droplet diameter for a 30% change in surface tension (e.g., 0.1 M DOC), resulting in a ca. 1% change in top-of-atmosphere albedo locally. However, a 15% decrease in surface tension for a 0.01 M DOC is probably the upper limit of the surface tension effects consistent with our measurements in the Amazon Basin. The intensive appearance of small organic fragments (i.e., C_xH_y-; x < 3, y < 7) and the lack of phosphate-containing compounds (i.e., phospholipids) in the fine-mode wet-season Amazonian aerosols [*Wouters et al.*, 1993] suggests a secondary biogenic origin. Organic compounds associated with secondary aerosol, such as mono- and dicarboxylic acids, show less surface tension effects than polyacidic substances [*Facchini et al.*, 2000].

6. Conclusions

[45] Based on the measured physical and chemical properties of wet-season aerosol in the Amazon Basin, the sulfate mass fraction could account for most of the CCN activity. However, uncertainty about the chemical speciation
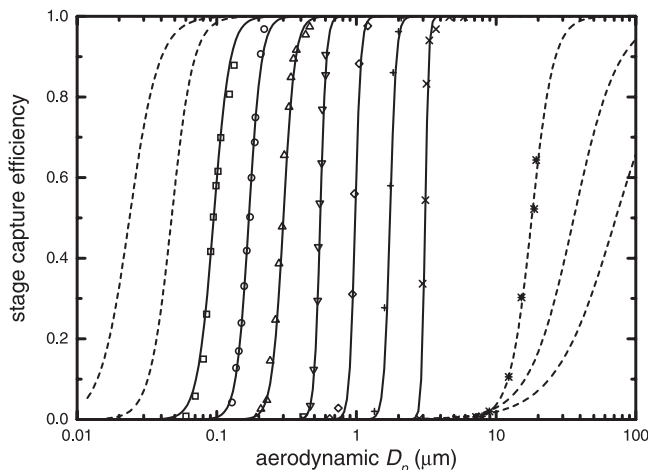

Figure A.1. Calibrated efficiency functions for the symmetric curve (A.4). The dotted curves correspond to the artificial stages.

Table A.1. Calibrated MOUDI Impactor Parameters for Nonlinear Inversion Routine

Stage number	D_{50}[a] (St_{50})	D_{50}[b] (manufactured)	s
11[c]	–	72	1.6
10[c]	–	36	2.7
9[c]	–	18	4.6
8	3.62	3.20	17.3
7	2.03	1.80	10.0
6	1.13	1.00	10.9
5	0.633	0.560	10.4
4	0.373	0.330	5.3
3	0.198	0.175	4.9
2	0.105	0.093	3.8
1[c]	–	0.047	2.9
0[c]	–	0.023	2.2

Abbreviation: s, steepness parameter.
[a]Calculated from theory (St_{50} = Stokes number for D_{50}).
[b]Values given for manufactured version of our impactor.
[c]Fictitious stages used for extrapolation.

and the solubility of the large organic component precludes a rigorous analysis of its contribution to nucleation activity. Within reasonable characterization of the organic component, we can predict a similar contribution to CCN activity from WSOC as that from the soluble inorganic component. A parameterization of the aerosol properties that control CCN activity shows that measuring the number distribution and surface tension effects are relatively more important than precisely determining the soluble content. The additional dissolution of water-soluble compounds will not dramatically effect resulting wet-season CCN spectra and a 15% decrease in surface tension is probably the upper limit of surface tension effects consistent with our wet-season measurements in the Amazon Basin.

Appendix A.

[46] Recovering the mass distribution, $f(D_p)$, involves solving the Fredholm equation of the first kind for each impactor stage. The measured mass on an impactor stage i, m_i, is approximated by integrating the product of the ith stage's kernel function, $k_i(D_p)$, and the jth iteration of the mass distribution, $f_j(D_p)$,

$$m_{ij}(D_p) = \sum_{p=1}^{x} k_i(D_p) f_j(D_p) \delta \log D_p \qquad (A.1)$$

where $m_{ij}(D_p)$ is the calculated mass for stage i and iteration step j, D_p the particle diameter at array number p, and x is the resolution at which the size distribution is evaluated, typically $x = 200$. The mass distribution, $f_{j+1}(D_p)$,

$$f_{j+1}(D_p) = f_j(D_p) \left[1 + a_i(D_p) \left(\frac{m_i}{m_{ij}} - 1 \right) \right] \qquad (A.2)$$

is solved iteratively by multiplying the previous iteration's mass distribution, $f_j(D_p)$ to the product of a weighting function, $a_i(D_p)$, and an expression containing the ratio of the actual mass to the calculated mass.

[47] Since the MOUDI impactor has narrow kernel functions, direct weighting of the correction factor with these functions tends to introduce the structure of the kernel
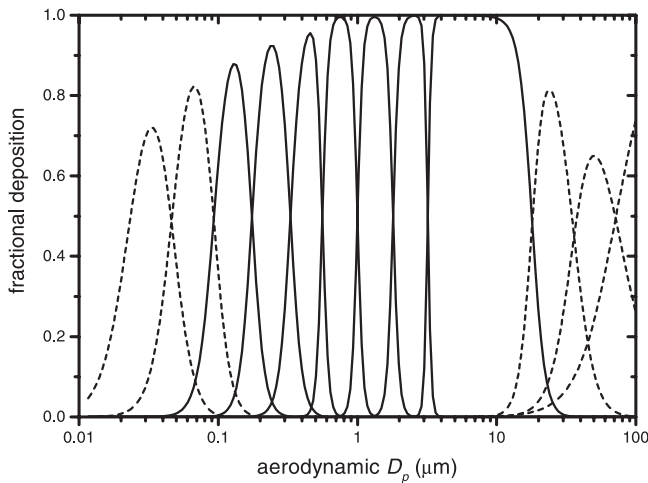
Figure A.2. Kernel functions for the manufactured version of the MOUDI impactor. The dotted curves correspond to the artificial stages.

functions in the resulting distribution. Hence, a weighting function proposed by WWJ90 was defined as

$$a_i(D_p) = \left\{ \frac{k_i(D_p)}{\max[k_i(D_p)]} \right\}^r \tag{A.3}$$

The exponent r ranged between 0.3 and 0.7; a value of 0.7 produced the best results and was used for our inversions.

[48] Smooth kernel curves for the MOUDI are derived by fitting a s-shaped function to the calibrated stage collection efficiency (Figure A.1) reported by *Marple et al.* [1991]. The efficiency curves for each stage were estimated using

$$E(D_p) = \left[1 + \left(\frac{D_{50}}{D_p} \right)^{2s} \right]^{-1} \tag{A.4}$$

where D_p is the particle diameter, D_{50} is the 50% cutpoint, and s is the steepness factor; the values of these parameters

are reported in Table A.1. The kernel functions, shown in Figure A.2, are derived from the efficiency curves in the order of the largest to smallest stage using the following expressions:

$$k_i(D_p) = E_i(D_p) \tag{A.5}$$

$$k_n(D_p) = E_n(D_p)\left[1 - E_{i+1}(D_p)\right] \times \ldots \times \left[1 - E_n(D_p)\right] \tag{A.6}$$

where $i = n - 1, n - 2, \ldots, 1$; n = number of stages.

[49] There is a lack of information at the endpoints, which makes it difficult to extrapolate the distribution beyond the D_{50s} of the first and last stages. Therefore, artificial stages (stages 0, 1, 9, 10, 11) were introduced with the characteristics of the real stages. For the MOUDI impactor, stage 9 is the inlet stage, which we did not analyze, but the steepness factor for this stage is known. The steepness values for the other fictitious stages were estimated by a power log extrapolation from the previous stages. The only purpose of this method is to provide a continuation of the first-guess distribution.

[50] Estimates for the fictitious stage loadings were calculated using multimodal lognormal distributions that best represent the measured mass distribution of each component. This lognormal estimation procedure for the first-guess distribution is the primary difference between this inversion technique and that of WWJ90. A multimodal mass distribution is described by the following expression:

$$\frac{\delta M}{\delta \log D_p} = \sum_{a=1}^{b} \frac{M_a}{\sqrt{2\pi} \ln \sigma_a} \exp\left[\frac{-(\ln D_p - \ln D_{pg,a})^2}{2\ln^2 \sigma_a} \right] \tag{A.7}$$

where M_a is the mass of a component, $D_{pg,a}$ is the median diameter, σ_a is the geometric standard deviation for a given mode a, and b is the number of modes. A maximum of two modes were used to describe the mass distributions and the parameters of the lognormal approximations are shown in Table A.2.

[51] Integration between the D_{50s} of the artificial stages yields the estimated mass for the first-guess distribution.

Table A.2. Parameter for Multimodal Lognormal Distributions (A.7) that Represent the Data Presented in Table 3

Component		first mode			second mode		
		M_1 (ng m^{-3})	$D_{pg,1}$ (μm)	$\sigma_{g,1}$	M_2 (ng m^{-3})	$D_{pg,2}$ (μm)	$\sigma_{g,2}$
Average	mass	2151	0.35	1.77	16066	4.29	2.04
	sulfate	399	0.33	1.57	266	3.43	2.43
	oxides	1581	2.99	2.48	–	–	–
MD_4	mass	2514	0.29	1.84	11254	3.85	2.16
	sulfate	389	0.31	1.64	241	3.20	2.36
	oxides	1218	3.06	2.50	–	–	–
MD_6	mass	2158	0.37	1.80	15717	4.55	1.96
	sulfate	240	0.34	1.51	181	4.11	2.07
	oxides	950	4.30	2.35	–	–	–
MD_9	mass	1872	0.39	1.64	16325	4.24	1.97
	sulfate	364	0.32	1.56	254	3.30	2.36
	oxides	1535	2.70	2.56	–	–	–
MD_10	mass	1888	0.35	1.60	21043	4.33	2.10
	sulfate	585	0.35	1.55	415	3.16	3.01
	oxides	2669	2.70	2.46	–	–	–

M_i is the mass for mode i, D_{pg} is the geometric median diameter, and $\sigma_{g,i}$ is the geometric standard deviation for mode i.

Stages were not allowed to be less than 10% of the adjacent stages in order to provide some continuity to the inversion routine. This constraint did not effect the measured size distribution, but often increased the estimated loading for the fictitious stages at the tail of the lognormal distribution. A three-term moving average was used to smooth the first-guess distribution, $f_0(D_p)$:

$$f_0(D_p) = 0.25 f_0(D_{p-1}) + 0.5\, f_0(D_p) + 0.25\, f_0(D_{p+1}) \quad (A.8)$$

$$f_0(D_1) = 0.75\, f_0(D_1) + 0.25\, f_0(D_2) \quad (A.9)$$

$$f_0(D_x) = 0.75\, f_0(D_x) + 0.25\, f_0(D_{x-1}) \quad (A.10)$$

where p are array numbers along the size distribution up to the x values in the array.

[52] The size distribution is calculated between one half D_{50} of stage 0 and two times D_{50} of stage 11, but the results are used between one half the D_{50} of the smallest MOUDI stage (2) and two times that of the largest stage. The stages 1 through 9 were included in the iteration process. The iteration was complete when the error parameter (ζ) was less than five percent. The error parameter used by WWJ90 was defined as

$$\xi^2 = \frac{1}{n} \sum_{i=1}^{n} \left[\frac{m_i - m_{ij}}{\delta m_i} \right]^2 \quad (A.11)$$

where δm_i is the absolute uncertainty for the mass on stage i, and n is the number of stages. m_i and m_{ij} are the measured and calculated mass loadings on stage i, respectively. Only the measured stages (2–8) determined the stopping criteria.

Appendix B: Definition of Variables

$a_i(D_p)$	kernel weighting function for stage i
D_{50}	50% cutoff wet diameter
d_{50}	50% cutoff dry diameter
D_p	wet particle diameter
d_p	dry particle diameter
D_{pc}	critical droplet diameter
d_{pg}	geometric median particle diameter
$E_i(D_p)$	efficiency function for MOUDI stage i
$f_{CCN/CN}$	fraction of aerosol that serve as CCN
$f_j(D_p)$	inverted mass distribution for iteration j
k	Boltzmann constant
$k_i(D_p)$	kernel function for stage I
M	aerosol mass concentration
M_i	molecular weight of species i
m_i	mass of species i
M_w	molecular weight of water
N	aerosol number concentration
n	number of MOUDI stages
N_{3010}	measured N from the CPC_{3010}
N_{CCN}	CCN concentration
N_{DMPS}	integrated N from DMPS measurements of $n_N(d_p)$
$n_M(D_p)$	mass distribution (wet diameter)
$n_M(d_p)$	mass distribution (dry diameter)
$n_N(d_p)$	number distribution (dry diameter)
N_R	Reference N_{CCN}
N_X	N_{CCN} at X% S_c
N_Δ	N_{CCN} for parameter change
RH	relative humidity
s	steepness factor
S_c	critical supersaturation
St_{50}	Stokes number for D_{50}
S_v	supersaturation
S_v^{eq}	equilibrium supersaturation
T	temperature
$\Delta\sigma'/\sigma'$	change in surface tension
Φ	osmotic coefficient
δ_S	relative change in CCN spectra
ν_i	van't Hoff factor
ρ'	density of aqueous solution
ρ_i	density of species i
ρ_w	density of water
σ'	surface tension of solution
σ_g	geometric standard deviation
ζ	stopping error parameter

References

Andreae, M. O., and T. W. Andreae, The cycle of biogenic sulfur compounds over the Amazon Basin, I, Dry season, *J. Geophys. Res.*, *93*, 1487–1497, 1988.

Andreae, M. O., H. Berresheim, H. Bingemer, D. J. Jacob, B. L. Lewis, S.-M. Li, and R. W. Talbot, The atmospheric sulfur cycle over the Amazon Basin, 2, Wet season, *J. Geophys. Res.*, *95*, 16,813–16,824, 1990a.

Andreae, M. O., R. W. Talbot, H. Berresheim, and K. M. Beecher, Precipitation chemistry in central Amazonia, *J. Geophys. Res.*, *95*, 16,987–16,999, 1990b.

Artaxo, P., and H. C. Hansson, Size distribution of biogenic aerosol particles from the Amazon Basin, *Atmos. Environ.*, *29*, 393, 1995.

Artaxo, P., and W. Maenhaut, Trace element concentrations and size distributions of biogenic aerosols from the Amazon Basin during the wet season, *Nucl. Instrum. Methods Phys. Res. Sect. B*, *49*, 366–371, 1990.

Artaxo, P., and C. Orsini, PIXE and receptor models applied to remote aerosol source apportionment in Brazil, *Nucl. Instrum. Methods Phys. Res. Sect. B*, *22*, 259–263, 1987.

Artaxo, P., H. Storms, F. Bruynseels, R. Van Grieken, and W. Maenhaut, Composition and sources of aerosols from the Amazon Basin, *J. Geophys. Res.*, *93*, 1605–1615, 1988.

Basset, M. E., and J. H. Seinfeld, Atmospheric equilibrium model of sulfate and nitrate aerosols, II, Particle size analysis, *Atmos. Environ.*, *18*, 1163–1170, 1984.

Bower, K. N., and T. W. Choularton, Cloud processing of the cloud condensation nucleus spectrum and its climatological consequences, *Q. J. R. Meteorol. Soc.*, *119*, 655, 1993.

Cruz, C., and S. Pandis, The effect of organic coatings on the cloud condensation nuclei activation of inorganic atmospheric aerosol, *J. Geophys. Res.*, *103*, 13,111–13,123, 1998.

Facchini, M., S. Decesari, M. Mircea, S. Fuzzi, and G. Loglio, Surface tension of atmospheric wet aerosol and cloud/fog droplets in relation to their organic carbon content and chemical composition, *Atmos. Environ.*, *34*, 4853–4857, 2000.

Facchini, M. C., M. Mircea, S. Fuzzi, and R. J. Charlson, Cloud albedo enhancement by surface-active organic solutes in growing droplets, *Nature*, *401*, 257–259, 1999.

Gerab, F., P. Artaxo, R. Gillet, and G. Ayers, PIXE, PIGE and ion chromatography of aerosol particles from northeast Amazon Basin, *Nucl. Instrum. Methods Phys. Res. Sect. B*, *138*, 955–960, 1998.

Graham, B., O. L. Mayol-Bracero, P. Guyon, G. C. Roberts, S. Decesari, M. C. Facchini, P. Artaxo, W. Maenhaut, P. Köll, and M. Andreae, Water-soluble organic compounds in biomass burning aerosols over Amazonia,

1, Characterization by NMR and GC-MS, *J. Geophys. Res.*, *107*, 10.1029/2001JD000033, in press, 2002.

Hoppel, W. A., J. W. Fitzgerald, G. M. Frick, R. E. Larson, and E. J. Mack, Aerosol size distributions and optical properties found in the marine boundary layer over the Atlantic Ocean, *J. Geophys. Res.*, *95*, 3659–3686, 1990.

Johansson, S., and J. Campbell, *PIXE: A Novel Technique for Elemental Analysis*, John Wiley, New York, 1988.

Kaufman, Y. J., and D. Tanré, Effect of variations in supersaturation on the formation of cloud condensation nuclei, *Nature*, *369*, 45–48, 1994.

Kavouras, I. G., N. Mihalopoulos, and E. G. Stephanou, Formation of atmospheric particles from organic acids produced by forests, *Nature*, *395*, 683–686, 1998.

Lala, G. G., and J. E. Jiusto, An automatic light scattering CCN counter, *J. Appl. Meteorol.*, *16*(4), 413–418, 1977.

Lide, D., *CRC Handbook of Chemistry and Physics*, CRC Press, Boca Raton, Fla., 2000.

Liu, P. S. K., W. R. Leaitch, C. M. Banic, and S.-M. Li, Aerosol observations at Chebogue Point during the 1993 North Atlantic Regional Experiment: Relationships among cloud condensation nuclei, size distribution, and chemistry, *J. Geophys. Res.*, *101*, 28,971–28,990, 1996.

Marple, V., K. Rubow, and S. Behm, A micro-orifice uniform deposit impactor (MOUDI): Description, calibration, and use, *Aerosol Sci. Technol.*, *14*, 434–446, 1991.

Mason, B., *Principles of Geochemistry*, John Wiley, New York, 1966.

Mayol-Bracero, O. L., P. Guyon, B. Graham, G. Roberts, M. O. Andreae, S. Decesari, M. C. Facchini, and S. Fuzzi, Water-soluble organic compounds in biomass burning aerosols over Amazonia, 2, Apportionment of the chemical compositon and importance of the polyacidic fraction, *J. Geophys. Res.*, *107*, 10.1029/2001JD000522, 2002a.

Mayol-Bracero, O. L., R. Gabriel, M. O. Andreae, T. W. Kirchstetter, T. Novakov, J. A. Ogren, P. J. Sheridan, and D. Streets, Carbonaceous aerosols over the Indian Ocean during INDOEX: Chemical characterization, optical properties, and probable sources, *J. Geophys Res.*, *107*, 10.1029/2000JD000039, in press, 2002b.

McInnes, L., P. Quinn, D. Covert, and T. Anderson, Gravimetric analysis, ionic composition, and associated water mass of the marine aerosol, *Atmos. Environ.*, *30*, 869–884, 1996.

Nenes, A., P. Chuang, R. Flagan, and J. Seinfeld, A theoretical analysis of cloud condensation nucleus (CCN) instruments, *J. Geophys. Res.*, *106*, 3449–3474, 2001.

Novakov, T., and C. E. Corrigan, Cloud condensation nucleus activity of the organic component of biomass smoke particles, *Geophys. Res. Lett.*, *23*, 2141–2144, 1996.

Novakov, T., and J. E. Penner, Large contribution of organic aerosols to cloud-condensation-nuclei concentrations, *Nature*, *365*, 823–826, 1993.

O'Dowd, C., J. Lowe, and M. Smith, Observations and modelling of aerosol growth in marine stratocumulus: Case study, *Atmos. Environ.*, *33*, 3053–3062, 1999.

Pruppacher, H. R., and J. D. Klett, *Microphysics of Clouds and Precipitation*, Kluwer Acad., Norwell, Mass., 1997.

Reid, J. S., and P. V. Hobbs, Physical and optical properties of young smoke from individual biomass fires in Brazil, *J. Geophys. Res.*, *103*, 32,013–32,030, 1998.

Rivera-Carpio, C. A., C. E. Corrigan, T. Novakov, J. E. Penner, C. F. Rogers, and J. C. Chow, Derivation of contributions of sulfate and carbonaceous aerosols to cloud condensation nuclei from mass size distributions, *J. Geophys. Res.*, *101*, 19,483–19,493, 1996.

Roberts, G., *Cloud Condensation Nuclei in the Amazon Basin: Their Role in a Tropical Rainforest*, Calif. Inst. Technol., Pasadena, Calif., 2001.

Roberts, G., J. Zhou, P. Artaxo, and M. Andreae, Cloud condensation nuclei in the Amazon Basin: "Marine" conditions over a continent?, *Geophys. Res. Lett.*, *28*, 2807–2810, 2001.

Saxena, P., and L. M. Hildemann, Water soluble organics in atmospheric particles: A critical review of the literature and application of thermodynamics to identify candidate compounds, *J. Atmos. Chem.*, *24*(1), 57–109, 1996.

Seinfeld, J. H., and S. N. Pandis, *Atmospheric Chemistry and Physics: From Air Pollution to Climate Change*, 1326 pp., John Wiley, New York, 1998.

Shulman, M. L., M. C. Jacobson, R. J. Charlson, R. E. Synovec, and T. E. Young, Dissolution behavior and surface tension effects of organic compounds in nucleating cloud droplets, *Geophys. Res. Lett.*, *23*, 277–280, 1996.

Swietlicki, E., et al., A closure study of sub-micrometer aerosol particle hygroscopic behaviour, *Atmos. Res.*, *50*, 205–240, 1999.

Talbot, R. W., M. O. Andreae, T. W. Andreae, and R. C. Harriss, Regional aerosol chemistry of the Amazon Basin during the dry season, *J. Geophys. Res.*, *93*, 1499–1508, 1988.

Talbot, R. W., M. O. Andreae, H. Berresheim, P. Artaxo, M. Garstang, R. C. Harriss, K. M. Beecher, and S. M. Li, Aerosol chemistry during the wet season in Central Amazonia: The influence of long-range transport, *J. Geophys. Res.*, *95*, 16,955, 1990.

Williams, M. R., T. R. Fisher, and J. M. Melack, Chemical composition and deposition of rain in the central Amazon, Brazil, *Atmos. Environ.*, *31*, 207, 1997.

Winklmayr, W., H.-C. Wang, and W. John, Adaptation of the Twomey algorithm to the inversion of cascade impactor data, *Aerosol Sci. Technol.*, *13*, 322–331, 1990.

Wouters, L., S. Hagedoren, I. Dierck, P. Artaxo, and R. V. Grieken, Laser microprobe mass analysis of Amazon Basin aerosols, *Atmos. Environ.*, *27A*, 661–668, 1993.

Zhou, J., E. Swietlicki, H. Hansson, and P. Artaxo, Sub-micrometer aerosol particle size distribution and hygroscopic growth measurements in the Amazonian rain forest during the wet season, *J. Geophys. Res.*, *107*, 10.1029/2000JD000203, in press, 2002.

———————

M. O. Andreae, Biogeochemistry Department, Max Planck Institute for Chemistry, Mainz, Germany.

G. C. Roberts, Department of Environmental Engineering, MC 138-78, California Institute of Technology, 1200 E. California Boulevard, Pasadena, CA 91125, USA. (groberts@cco.caltech.edu)

P. Artaxo, University of São Paulo, São Paulo, Brazil.

E. Swietlicki and J. Zhou, University of Lund, Lund, Sweden.